On the damped oscillations of an elastic quasi-circular membrane in a two-dimensional incompressible fluid

Marco Martins Afonso, Simon Mendez, Franck Nicoud

▶ To cite this version:

Marco Martins Afonso, Simon Mendez, Franck Nicoud. On the damped oscillations of an elastic quasi-circular membrane in a two-dimensional incompressible fluid. Journal of Fluid Mechanics, 2014, 746, pp.300 -331. 10.1017/jfm.2014.135 . hal-00957710

HAL Id: hal-00957710

https://hal.science/hal-00957710

Submitted on 10 Mar 2014

On the damped oscillations of an elastic quasi-circular membrane in a two-dimensional incompressible fluid

By Marco Martins Afonso[1,2], Simon Mendez[1] and Franck Nicoud[1]

[1]Institut de Mathématiques et de Modélisation de Montpellier, CNRS UMR 5149,
Université Montpellier 2, c.c.051, 34095 Montpellier cedex 5, France

[2]Laboratoire de Mécanique, Modélisation et Procédés Propres, CNRS UMR 7340,
Aix-Marseille Université, Ecole Centrale Marseille, 13451 Marseille cedex 13, France

(Received 13 January 2014)

We propose a procedure — partly analytical and partly numerical — to find the frequency and the damping rate of the small-amplitude oscillations of a massless elastic capsule immersed in a two-dimensional viscous incompressible fluid. The unsteady Stokes equations for the stream function are decomposed onto normal modes for the angular and temporal variables, leading to a fourth-order linear ordinary differential equation in the radial variable. The forcing terms are dictated by the properties of the membrane, and result into jump conditions at the interface between the internal and external media. The equation can be solved numerically, and an excellent agreement is found with a fully-computational approach we developed in parallel. Comparisons are also shown with the results available in the scientific literature for drops, and a model based on the concept of entrained fluid is presented, which allows for a good representation of the results and a consistent interpretation of the underlying physics.

1. Introduction

During the last two decades, numerical simulations of deformable particles in flows have received increasing attention. Several numerical methods have been developed to predict the dynamics of particles composed by a drop of liquid enclosed in a membrane, or more generally in a flexible structure. Different particles are described by this model, such as biological cells (typically red blood cells), lipid vesicles or elastic capsules. Such particles are small (their diameter is of the order of a few microns) and they often evolve in creeping flows, well described by the Stokes equations. Taking advantage of the linearity of the Stokes equations, boundary integral methods (BIM) (Pozrikidis, 1992, 2010) are efficient techniques to solve the dynamics of fluidic particles in an external flow. These methods have been successfully applied to red blood cells (Pozrikidis, 1995; Zhao *et al.*, 2010; Zhao & Shaqfeh, 2011; Peng *et al.*, 2011), capsules (Lac *et al.*, 2007; Walter *et al.*, 2011; Hu *et al.*, 2012) and vesicles (Ghigliotti *et al.*, 2010; Veerapaneni *et al.*, 2011; Biben *et al.*, 2011; Sohn *et al.*, 2010; Boedec *et al.*, 2012). One of the appealing features of BIM is that they do not need the discretisation of the fluid domain (Pozrikidis, 1992).

However, as recently stressed by Salac & Miksis (2012), vesicles (and other similar cells) sometimes evolve in flows where inertia cannot be neglected. As far as red blood cells are concerned, the particle Reynolds number — i.e., the one based on the red blood cell size and the local velocity gradient — is generally small under normal physiological conditions. However, non-physiological flows are prime examples where cells are submitted to extreme stress conditions. In ventricular assist devices, the Reynolds number can reach values of 10^4 or 10^5 (Fraser *et al.*, 2011), potentially resulting in blood damage. In such conditions, the flow cannot be described by the Stokes equations. The applicability of the BIM to the Navier–Stokes equations and to the unsteady Stokes equations has been demonstrated (Greengard & Kropinski, 1998; Jiang *et al.*, 2013). However, in the context of flows of vesicles, capsules or cells, the BIM is mainly used for creeping flows.

Alternative numerical methods able to predict flow-induced deformations of fluid particles enclosed by a membrane in regimes where the Reynolds number is not zero have been developed in recent years (Peskin, 2002; Lee & Leveque, 2003; Le *et al.*, 2006; Cottet & Maitre, 2006; Kim & Lai, 2010; Salac & Miksis, 2011; Yazdani & Bagchi, 2013). Such methods are usually developed and tested in two dimensions before their adaptation to three dimensions. Quality assessment of these methods is of course essential. However, validation itself is an issue: while an experiment may mimic a two-dimensional flow, flowing particles are inherently 3-D. Likewise, owing to the moderate computational cost of BIM, reference numerical results generated by BIM are 3-D for the most part. The comparison of 2-D results and 3-D measurements or simulation results can only be qualitative, and does not constitute a true validation. However, some 2-D simulations using BIM are available in the literature (Breyiannis & Pozrikidis, 2000; Veerapaneni *et al.*, 2009; Ghigliotti *et al.*, 2010; Woolfenden & Blyth, 2011) and can be used for validation, in the Stokes regime. Validation in regimes where the flow cannot be described by the steady Stokes equation is more problematic. In such cases, numerical publications are generally limited to simulation feasibility and qualitative assessments, or comparisons only with similar methods: most of the methods developed to compute capsules or vesicles dynamics in flows with non-zero Reynolds number rely on diffuse interfaces, where the effect of the membrane is smoothed over several grid cells. Extensive validation of such methods is thus indispensable, and analytical results — necessary to properly discuss the pros and cons of new numerical methods — are missing.

The present paper represents an analytical investigation of a problem already faced several times numerically in literature, and is a step towards more extensive validation of 2-D numerical methods for simulations of fluid particle dynamics under flow. A normal-mode analysis is performed for the case of a two-dimensional capsule, enclosed by an elastic stretched membrane. A perturbation of the membrane equilibrium shape results in damped oscillations and relaxation to a circular state. Such a case has been used to illustrate the performances of 2-D numerical methods (Tu & Peskin, 1992; Lee & Leveque, 2003; Cottet & Maitre, 2006; Song *et al.*, 2008; Tan *et al.*, 2008), albeit without validating against analytical results.

Similar studies have been led for other deformable objects. The problem of oscillations of drops or vesicles has received substantial attention over the years (Lamb, 1932; Prosperetti, 1980*b*; Lu & Apfel, 1991; Rochal *et al.*, 2005). However, most of the approaches treat three-dimensional configurations, relevant of course to practical applications. The present paper provides semi-analytical results for the oscillating relaxation of two-dimensional capsules without external flow, and proposes a discussion on the similarities with the behaviour of droplets. We will also introduce a simple phenomenological model to explain the origin of the oscillations of a massless membrane immersed in a creeping flow.

The paper is organised as follows. In section 2 we sketch the problem under consideration. Section 3 shows the guidelines of the equations into play. In section 4 the main results are reported. Section 5 presents a discussion on similar systems and on physical models. Conclusions and perspectives follow in section 6. The appendices A, B and C are devoted to detailing the expression of the membrane elongation, the analytical procedure for our differential equations, and the numerical discretisation using finite differences, respectively. Our nomenclature and notation are recalled in tables 3–4.

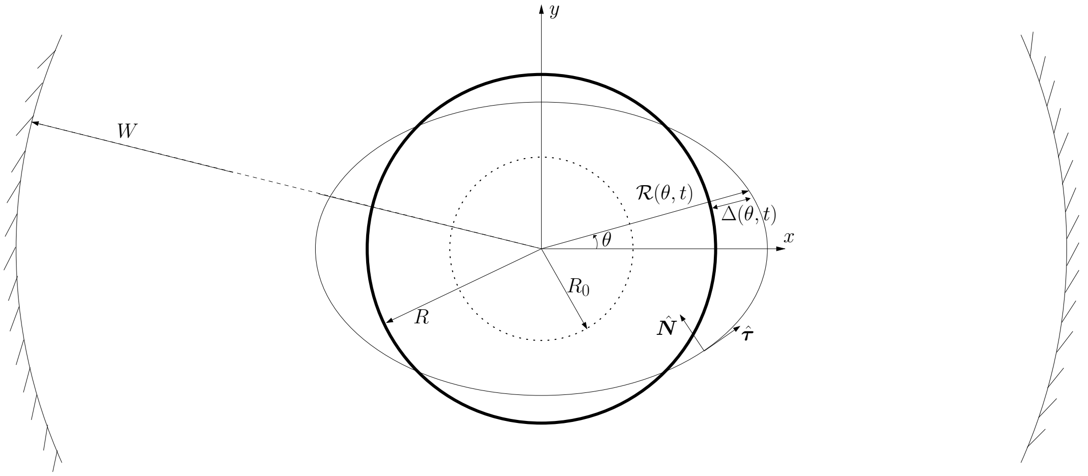

FIGURE 1. Sketch of the problem and of the notations for membrane, fluid and wall. The inflated membrane with radius R at rest oscillates within a circular fluid domain of radius W. The dotted circle represents the zero-stress configuration of the membrane of radius R_0 (non-inflated membrane).

2. Problem

Let us consider the motion of an elastic one-dimensional closed membrane, slightly deformed from its circular rest shape, immersed in — and thus also enclosing a portion of — a two-dimensional incompressible viscous fluid (figure 1). The membrane is pre-inflated, which means that the reference circle of radius R is not an unstressed shape. The unstressed shape is considered to be a circle of radius $R_0 < R$. The membrane is thus under tension even without deformation, and the incompressibility of the enclosed fluid prevents the membrane from reaching its unstressed shape. We study the time evolution of the membrane shape around the reference circle of radius R, focusing on the case of small-amplitude deformations, We can describe the problem in polar coordinates $\boldsymbol{r} = (r, \theta)$ via the membrane location $\mathcal{R}(\theta, t) = R + \Delta(\theta, t)$, where R is the radius of the aforementioned circle and $\Delta(\theta, t)/R \ll 1 \; \forall \; \theta, t$. This description of course neglects the membrane thickness and excludes those situations where the membrane folds, so that two or more membrane locations would be present at the same angle. We also introduce a long-wave hypothesis, in order to neglect the cases in which the instantaneous oscillations would be so spatially dense as to result in an interface almost oriented in the radial direction at the nodal points. Consequently, the local instantaneous curvature is defined as (Gray, 1997)

$$\Gamma(\theta,t)=\frac{\mathcal{R}^2+2\mathcal{R}'^2-\mathcal{R}\mathcal{R}''}{(\mathcal{R}^2+\mathcal{R}'^2)^{3/2}}=\frac{(R+\Delta)^2+2\Delta'^2-(R+\Delta)\Delta''}{[(R+\Delta)^2+\Delta'^2]^{3/2}}\ , \tag{2.1}$$

with the prime denoting a derivative with respect to θ.

In the spirit of a perturbative approach, the continuity and forced Navier–Stokes equations for the fluid velocity can be linearised around the reference state of fluid at rest, and the resulting equations for the perturbation $\boldsymbol{u}(r,\theta,t)=u_r\hat{\boldsymbol{e}}_r+u_\theta\hat{\boldsymbol{e}}_\theta$ read:

$$\frac{1}{r}\frac{\partial(ru_r)}{\partial r}+\frac{1}{r}\frac{\partial u_\theta}{\partial\theta}=0\ , \tag{2.2}$$

$$\rho\frac{\partial u_r}{\partial t}=-\frac{\partial p}{\partial r}+\nu\left(\frac{\partial^2u_r}{\partial r^2}+\frac{1}{r}\frac{\partial u_r}{\partial r}+\frac{1}{r^2}\frac{\partial^2u_r}{\partial\theta^2}-\frac{u_r}{r^2}-\frac{2}{r^2}\frac{\partial u_\theta}{\partial\theta}\right)+\delta(r-\mathcal{R})f_r\ , \tag{2.3}$$

$$\rho\frac{\partial u_\theta}{\partial t}=-\frac{1}{r}\frac{\partial p}{\partial\theta}+\nu\left(\frac{\partial^2u_\theta}{\partial r^2}+\frac{1}{r}\frac{\partial u_\theta}{\partial r}+\frac{1}{r^2}\frac{\partial^2u_\theta}{\partial\theta^2}-\frac{u_\theta}{r^2}+\frac{2}{r^2}\frac{\partial u_r}{\partial\theta}\right)+\delta(r-\mathcal{R})f_\theta\ , \tag{2.4}$$

where ρ and ν are the (constant) mass density and kinematic viscosity, respectively, p is the fluid pressure, and the non-linear inertial terms (quadratic coupling of $\boldsymbol{u}$ with itself) have been consistently dropped.

The linear force per unit volume, $\boldsymbol{f}(\theta,t)=f_r\hat{\boldsymbol{e}}_r+f_\theta\hat{\boldsymbol{e}}_\theta$, exerted by the membrane on the fluid, can easily be expressed in the reference frame defined by the unit vectors locally counterclockwise-tangential and inward-normal to the interface, $\hat{\boldsymbol{\tau}}$ and $\hat{\boldsymbol{N}}$ respectively (see figure 1). In terms of the local instantaneous elongation $\chi(\theta,t)$ of the membrane (to be defined in (2.9) and discussed in appendix A), this force reads (Breyiannis & Pozrikidis, 2000)

$$\boldsymbol{f}=E\left(\frac{\mathrm{d}\chi}{\mathrm{d}\tau}\hat{\boldsymbol{\tau}}+\chi\Gamma\hat{\boldsymbol{N}}\right)\ , \tag{2.5}$$

where $\mathrm{d}/\mathrm{d}\tau$ is the curvilinear derivative following $\hat{\boldsymbol{\tau}}$,

$$\frac{\mathrm{d}}{\mathrm{d}\tau} = [(R+\Delta)^2 + \Delta'^2]^{-1/2} \frac{\partial}{\partial\theta} \; , \tag{2.6}$$

and E is an elastic modulus representing the membrane thickness times its Young modulus and is considered as constant in the limit of vanishing thickness. The pairs of polar and curvilinear unit vectors are related to each other by

$$\hat{\boldsymbol{\tau}} = [(R+\Delta)^2 + \Delta'^2]^{-1/2} \, [\Delta' \hat{\boldsymbol{e}}_r + (R+\Delta)\hat{\boldsymbol{e}}_\theta] \tag{2.7}$$

and

$$\hat{\boldsymbol{N}} = [(R+\Delta)^2 + \Delta'^2]^{-1/2} \, [-(R+\Delta)\hat{\boldsymbol{e}}_r + \Delta' \hat{\boldsymbol{e}}_\theta] \; . \tag{2.8}$$

The membrane elongation appearing in (2.5) is defined as

$$\chi(\theta, t) = \frac{L(\theta,t) - L_0}{L_0} \; , \tag{2.9}$$

L being the length of an infinitesimal membrane arc and L_0 its deflated value in the zero-stress configuration, which will actually disappear from the final expression. As shown in appendix A, such a definition makes the membrane elongation characterised by a transport equation. The membrane elongation thus depends not only on the membrane location $\mathcal{R}(\theta, t)$, but also on the dynamical state, through the appearance of the fluid velocity. By decomposing the elongation into a mean constant part — averaged on the angle and denoted by a bar — and a fluctuating one (small by definition, with zero angular average and denoted by a tilde), we have:

$$\chi(\theta,t) = \bar{\chi} + \tilde{\chi}(\theta,t) \; , \qquad \bar{\chi} = \frac{R - R_0}{R_0} \; . \tag{2.10}$$

Moreover, the Dirac deltas in (2.3–2.4) indicate that the force in (2.5) only acts at the local and instantaneous membrane location, $r = \mathcal{R}(\theta, t)$. However, in the limit of small-amplitude deformations, this differs only slightly from the circle $r = R$, and at the leading order in Δ/r all the relevant expressions (and consequently (2.5)) can be simplified by expanding them around the reference state:

$$\begin{aligned}
&\Gamma(\theta,t) \simeq \frac{1}{R}\left(1-\frac{\Delta}{R}-\frac{\Delta''}{R}\right) \;, \\
&\frac{\mathrm{d}}{\mathrm{d}\tau} \simeq \frac{1}{R}\left(1-\frac{\Delta}{R}\right)\frac{\partial}{\partial\theta} \;, \\
&\delta(r-\mathcal{R}) \simeq \delta(r-R) - \Delta\dot{\delta}(r-R) \;, \\
&\hat{\boldsymbol{\tau}} \simeq \frac{\Delta'}{R}\hat{\boldsymbol{e}}_r + \hat{\boldsymbol{e}}_\theta \;, \\
&\hat{\boldsymbol{N}} \simeq -\hat{\boldsymbol{e}}_r + \frac{\Delta'}{R}\hat{\boldsymbol{e}}_\theta \;.
\end{aligned} \tag{2.11}$$

In the limit of small-amplitude deformations, the transport equation for the membrane elongation reads (see appendix A for details):

$$\frac{\partial\tilde{\chi}(\theta,t)}{\partial t} = \frac{\bar{\chi}+1}{R}\left[\frac{\partial u_\theta}{\partial\theta}+u_r\right](R,\theta,t) \;. \tag{2.12}$$

Notice that, for the above simplifications to hold, there is no need for the angular derivatives to be small, but simply “not to be large”, which is a much weaker request. In other words, our long-wave hypothesis corresponds to the assumption that the $\partial/\partial\theta$ operator (along with its square) does not increase the order of magnitude of any quantity, so that if something is small then the same is true for its first and second derivatives with respect to θ.

Expression (2.5) incorporates both the normal force related to fluid pressure differences, and the tangential stress due to variations in the membrane local elongation. It is thus obvious that this will result in jump conditions, which in the same spirit should be imposed on the *fixed and known* reference circular state. They must be supplemented by the continuity of the velocity field,

$$u_r^- = u_r^+ \qquad \text{and} \qquad u_\theta^- = u_\theta^+ \;, \tag{2.13}$$

where $\cdot^\pm = \lim_{r\to R_\pm}\cdot$ and all equalities hold for any angle and time. The forthcoming partial differential equations will then hold separately in both the internal and the external fluid regions, and will have to be matched according with (2.13) and momentum-related jump conditions — as detailed in section 3.

Finally, boundary conditions must be imposed: both at the origin due to the polar-coordinate geometric constraint, and at the external wall (which may even be placed at infinity, but which in what follows will be considered as a concentric circle of radius $W > R$) because of the no-slip constraint:

$$u_r|_{r=0} = 0 = \left.\frac{\partial u_r}{\partial r}\right|_{r=0} , \qquad u_r|_{r=W} = 0 = u_\theta|_{r=W} \ . \tag{2.14}$$

This completes the basic picture of the physical system under investigation. It is however instructive to recast the problem in nondimensional form. With this aim, let us introduce (Prosperetti, 1980*b*) the membrane characteristic time

$$T = \sqrt{\frac{\rho}{E}\frac{R^3 R_0}{R - R_0}} \ , \tag{2.15}$$

and the so-called reduced viscosity, corresponding to the ratio between T itself and the viscous time scale R^2/ν:

$$\nu_* = \frac{\nu T}{R^2} = \sqrt{\frac{\nu \mu R_0}{ER(R - R_0)}} \tag{2.16}$$

(here $\mu = \rho\nu$ is the dynamic viscosity). A standard application of the well-known Vaschy–Buckingham π theorem tells us that the problem can be formulated in terms of two nondimensional quantities, which can be chosen as ν_* and the ratio $R_* = R_0/R$, as we will show at the end of section 3.

The membrane characteristic time T pilots the oscillatory part of the problem. The natural appearance of this elastic time scale makes it necessary to take the time dependence into account, even in the absence of any typical temporal scale induced by external forcing or fluid motion. This is why we decided to use the time-dependent Stokes equations — or equivalently the linearised Navier–Stokes equations — to describe a problem which is intimately unsteady. Notice that, in the presence of a massless membrane, neglecting the time derivative of the fluid velocity would imply the absence of any fluid inertia (after the cancellation of the quadratically-small advective term), therefore no oscillatory motion would be possible and the problem would reduce to a simple direct return towards the circular shape.

3. Equations

Let us start our analysis from the linearised forced Navier–Stokes equations. As the unperturbed flow is at rest, they are equivalent to the unsteady Stokes equations. Note that an option to tackle this problem would be to rely on a BIM for unsteady Stokes equations (Jiang *et al.*, 2012), which could also be used for more complex shapes. Here, we follow a different approach, taking advantage of the simplicity of the configuration. By taking the curl of the equations (2.3–2.4), we get rid of pressure in the equation:

$$\begin{aligned}\frac{\partial^2 u_r}{\partial\theta\partial t} - \frac{\partial}{\partial r}\left(r\frac{\partial u_\theta}{\partial t}\right) = \nu \Bigg\{ & \frac{\partial}{\partial\theta}\left[\frac{\partial^2 u_r}{\partial r^2} + \frac{1}{r}\frac{\partial u_r}{\partial r} + \frac{1}{r^2}\frac{\partial^2 u_r}{\partial\theta^2} - \frac{u_r}{r^2} - \frac{2}{r^2}\frac{\partial u_\theta}{\partial\theta}\right] \\ & -\frac{\partial}{\partial r}\left[r\frac{\partial^2 u_\theta}{\partial r^2} + \frac{\partial u_\theta}{\partial r} + \frac{1}{r}\frac{\partial^2 u_\theta}{\partial\theta^2} - \frac{u_\theta}{r} + \frac{2}{r}\frac{\partial u_r}{\partial\theta}\right]\Bigg\} \\ & +\frac{E}{\rho R_0}\left\{\left[\Delta'\left(1-\frac{R_0}{R}\right)\left(1-\frac{r}{R}\right) - \frac{rR_0}{R}\chi'\right]\dot{\delta}(r-R)\right. \\ & \left. + \left[\frac{\Delta'''}{R}\left(1-\frac{R_0}{R}\right) - 2\frac{R_0}{R}\chi'\right]\delta(r-R)\right\} \ . \end{aligned} \tag{3.1}$$

The superscript dot here denotes a derivative with respect to the argument itself of the delta. (Notice that (3.1) represents the equation for the vorticity field, multiplied by $-r$). This equation accounts for the linearisation of the fluid equations and of the membrane quantities, since the forcing terms in (2.3–2.4) were expressed through (2.5) and (2.11). The continuity equation (2.2) is automatically satisfied by introducing the stream function $\psi(r,\theta,t)$ such that

$$u_r = \frac{1}{r}\frac{\partial\psi}{\partial\theta} \ , \qquad u_\theta = -\frac{\partial\psi}{\partial r} \ . \tag{3.2}$$

We now perform a normal-mode analysis, i.e. we project onto a basis made up of complex exponentials in the angle and in time, in the form

$$\psi(r,\theta,t) = \sum_{n=-\infty}^{+\infty} \phi_n(r) \mathrm{e}^{\mathrm{i}(n\theta - \omega_n t)} \ , \tag{3.3}$$

coupled with an analogous expansion for the two relevant quantities pertaining to the membrane, viz. its deformation Δ and (from (2.10), the mean-free part of) its elongation $\tilde{\chi}$:

$$\Delta(\theta,t) = \sum_{n=-\infty}^{+\infty} \xi_n \mathrm{e}^{\mathrm{i}(n\theta - \omega_n t)} \ , \tag{3.4}$$

$$\tilde{\chi}(\theta,t) = \sum_{n\neq 0} \gamma_n \mathrm{e}^{\mathrm{i}(n\theta - \omega_n t)} \ . \tag{3.5}$$

Here, n is integer and ω_n complex. The real and imaginary parts of ω_n correspond to the angular frequency of the membrane oscillations and to the (opposite of the) damping rate due to viscous dissipative effects, respectively, for the mode n. Finding this complex parameter — common to both the membrane and the fluid — is our main objective, which also means that we renounce to impose any initial condition for the fluid motion, in the spirit of an eigenmode decomposition. For both this complex frequency and the amplitudes $\phi_n(r)$, ξ_n and γ_n, we drop the subscript n whenever unambiguous. The stream function ψ being defined up to an arbitrary additive constant (namely, a space-independent, but possibly time-dependent, term), the addend corresponding to $n = 0$ shows an undetermined degree of freedom $\phi(r) \mapsto \phi(r) + \text{constant}$. Due to the area-preservation constraint, this is only related to membrane rotation and angular momentum, because it gives rise to an azimuthal angle-independent flow $(u_r = 0, u_\theta(r,t))$. Therefore we decide to neglect the mode $n = 0$, as well as the modes $n = \pm 1$ which would imply a translation of the centre of mass. Even if a generic superposition of modes could be dealt with, here we mainly focus on an isolated mode at each time. For a single mode, the area preservation cannot hold exactly, but it does at working order, i.e. neglecting all quadratic amplitudes. Also notice that the following conjugation relations must hold, so as to ensure that ψ, Δ and $\tilde{\chi}$ are real quantities (namely, waves travelling in the azimuthal direction) upon summing the pairs of contributions with n and $-n$:

$$\phi_{-n} = \phi_n^\star \ , \qquad \xi_{-n} = \xi_n^\star \ , \qquad \gamma_{-n} = \gamma_n^\star \ , \qquad \omega_{-n} = -\omega_n^\star \ .$$

In fact, in this specific case, the symmetry is even stronger due to invariance by reflection (parity of (3.1) in θ and consequently of the upcoming (3.11–3.13) in n), so that already *for each single* n any solution ω_n has a twin solution with same imaginary part and opposite real one. As a consequence, the sum of the contributions from n and $-n$ in the series (3.3–3.5) actually consists of four addends, i.e. of two azimuthal waves travelling in opposite directions with the same speed and damping rate, which therefore interfere to produce a *stationary wave*.

Referring the details to appendix B, here we only mention that, after the appropriate substitutions, equation (3.1) can be recast in closed form by expressing the link between the membrane-related quantities Δ, χ and the fluid stream function ψ (or ϕ) itself. As a result, in each of the two domains $r < R$ and $r > R$, we have

$$\phi^{(4)} + \frac{2}{r}\phi^{(3)} + \left(-\frac{2n^2+1}{r^2} + \frac{\mathrm{i}\omega}{\nu}\right)\phi^{(2)} + \left(\frac{2n^2+1}{r^3} + \frac{\mathrm{i}\omega}{\nu r}\right)\phi^{(1)} + \left(\frac{n^4-4n^2}{r^4} - \frac{\mathrm{i}\omega n^2}{\nu r^2}\right)\phi = 0 \ , \tag{3.6}$$

with $^{(l)}$ denoting the l-th derivative with respect to r.

This must be supplemented with an appropriate rewriting of the constraints (2.13–2.14). The boundary conditions at the origin and at the (circular) wall imply the vanishing of both the function and of its first derivative at both ends, and read:

$$\phi|_{r=0} = 0 = \phi|_{r=W} \ , \qquad \phi^{(1)}|_{r=0} = 0 = \phi^{(1)}|_{r=W} \ . \tag{3.7}$$

The continuity of the fluid velocity at the membrane implies the same for the function and its first derivative:

$$\phi^{-} = \phi^{+} , \qquad \phi^{(1)-} = \phi^{(1)+} . \tag{3.8}$$

Pressure is no longer relevant in this formulation. However, the effect of the Dirac delta's from (2.3–2.4) is to provide additional jump conditions on the second and third derivative of ϕ at the interface, which complete (3.7–3.8) and can be derived by means of appropriate successive integrations (see appendix B for more details):

$$\phi^{(2)-} - \phi^{(2)+} = \frac{\mathrm{i}n^2 E}{\mu R_0 R^2 \omega} \left[\phi(R) - R\phi^{(1)}(R) \right] , \tag{3.9}$$

$$\phi^{(3)-} - \phi^{(3)+} = \frac{\mathrm{i}n^2 (n^2 - 1) E}{\mu R_0 R^3 \omega} \left(1 - \frac{R_0}{R} \right) \phi(R) . \tag{3.10}$$

Finally, let us first reformulate the problem in nondimensional fashion, as anticipated at the end of section 2. In other words, by using the nondimensionalised radial coordinate $r \mapsto r_* = r/R$ and angular frequency $\omega \mapsto \omega_* = \omega T$, and by exploiting (2.15–2.16), equation (3.6) and constraints (3.9–3.10) can be recast as:

$$\begin{aligned} &\phi^{(4)}(r_*) + \frac{2}{r_*}\phi^{(3)}(r_*) + \left(-\frac{2n^2+1}{r_*^2} + \frac{\mathrm{i}\omega_*}{\nu_*} \right) \phi^{(2)}(r_*) \\ &+ \left(\frac{2n^2+1}{r_*^3} + \frac{\mathrm{i}\omega_*}{\nu_* r_*} \right) \phi^{(1)}(r_*) + \left(\frac{n^4 - 4n^2}{r_*^4} - \frac{\mathrm{i}\omega_* n^2}{\nu_* r_*^2} \right) \phi(r_*) = 0 , \end{aligned} \tag{3.11}$$

$$\phi^{(2)-} - \phi^{(2)+} = \frac{\mathrm{i}n^2}{\omega_* \nu_* (1 - R_*)} \left[\phi(1) - \phi^{(1)}(1) \right] , \tag{3.12}$$

$$\phi^{(3)-} - \phi^{(3)+} = \frac{\mathrm{i}n^2 (n^2 - 1)}{\omega_* \nu_*} \phi(1) . \tag{3.13}$$

Notice that, due to the homogeneity of (3.7–3.8) and (3.11–3.13) in ϕ, it is not necessary to nondimensionalise this latter quantity, of dimension length squared over time. This means that, in units of T^{-1}, the oscillation frequency and the damping rate can be expressed as

$$\mathrm{Re}(\omega_*) = h(n, \nu_*, R_*) , \qquad \mathrm{Im}(\omega_*) = g(n, \nu_*, R_*) \tag{3.14}$$

by means of two unknown functions h and g, whose behaviour will be investigated numerically in section 4.

4. Results

In this section we show the analytical/numerical results for the real and imaginary parts of the nondimensional ω_*. A numerical procedure is indeed necessary to obtain the nondimensional functions h and g from (3.14). A standard finite-difference scheme is implemented, consisting in discretising the $r_* \in [0, W/R]$ domain with M points, in transforming (3.11) into a set of M coupled linear equations accordingly (with conditions (3.7–3.8) and (3.12–3.13)), and in finding the complex ω_* which annihilates the determinant of the matrix derived in this way. This was accomplished by developing a specific program in MATLAB. Details about the numerical procedure are provided in appendix C.

4.1. *Influence of domain size, wall conditions and mesh refinement*

The presence of an external wall of circular shape has been introduced in this work to allow comparisons with numerical simulations of the full fluid-structure interaction problem in confined environments. However, we will mainly show results relevant to the damped oscillations in an infinite medium. Our claim is that our results are generally valid also in the absence of this wall, and to state this we have to show two properties: first, that a saturation zone exists, in which the wall is far enough as not to substantially modify the results if it is moved further away (P1); second, that at this W it is indifferent to impose no-slip or free-slip wall conditions (P2). The latter constraint, instead of $u_\theta|_{r=W} = 0$, translates into the absence of any tangential stress:

$$0 = r\frac{\partial(u_\theta/r)}{\partial r}\bigg|_{r=W} + \frac{1}{r}\frac{\partial u_r}{\partial \theta}\bigg|_{r=W} = \phi^{(2)}(W) - \frac{1}{W}\phi^{(1)}(W) \; . \qquad (4.1)$$

Figure 2 shows how the real and imaginary parts of ω_* depend on W/R and the wall boundary condition, for the following values of the parameters: $n = 2$, $\nu_* = 0.001$ and $R_* = 0.5$. This case will be referred to as our reference case. Figure 2 shows that

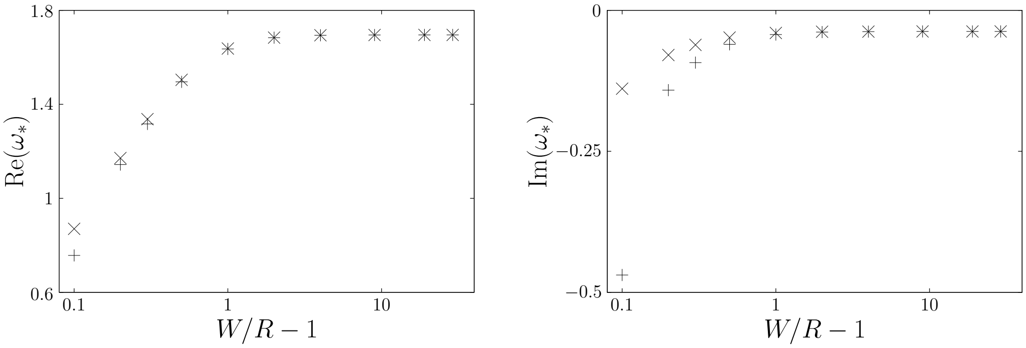

FIGURE 2. Behaviour of the real (left panel) and imaginary (right panel) parts of the complex nondimensional angular frequency ω_*, as a function of the nondimensional external wall radius $W/R-1$, for both the no-slip (+) and the free-slip (×) cases. Our working point for the subsequent calculations, $W/R-1=9$, lies in a range where saturation has taken place and the wall condition is irrelevant. The values of the other parameters are $n=2$, $\nu_*=0.001$ and $R_*=0.5$.

properties P1 and P2 are actually verified already at $W/R=10$ (our working point for the subsequent calculations). Differences in the real and imaginary parts of ω_* are less than 0.01% when W is changed from $W/R=10$ to $W/R=30$.

Finally, denoting the grid spacing by $\triangle r = W/(M-1)$, the result of a grid convergence study is displayed in figure 3. Grid convergence is shown for the real and imaginary parts of ω_* by constructing $\mathcal{E}_{\mathrm{Re}}$ and $\mathcal{E}_{\mathrm{Im}}$, which are relative errors with respect to our working point $\triangle r/R = 0.0001$, for which the complex nondimensional angular frequency is denoted ω_*^{WP}:

$$\mathcal{E}_{\mathrm{Re}}\left(\frac{\triangle r}{R}\right) = \frac{|\mathrm{Re}(\omega_*(\triangle r/R)) - \mathrm{Re}(\omega_*^{\mathrm{WP}})|}{|\omega_*^{\mathrm{WP}}|}. \tag{4.2}$$

The definition of $\mathcal{E}_{\mathrm{Im}}$ is obtained by substituting imaginary parts to real parts in (4.2). Results are almost independent of the grid size for sufficiently small grid spacing, but a non-monotonic convergence is observed, as shown by figure 3 (left). This may be related to the fact that the resolution of the numerical solutions and of the reference solution are too close. Memory constraints, notably, preclude the use of much finer discretization.

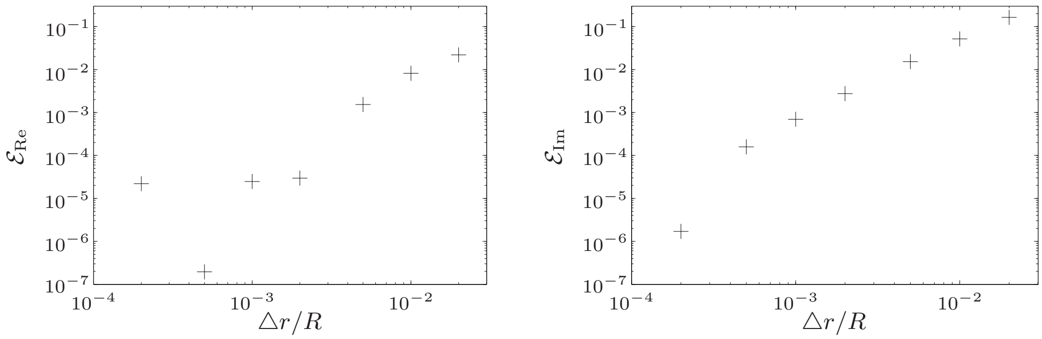

FIGURE 3. Grid convergence of the real (left panel) and imaginary (right panel) parts of ω_* as a function of $\triangle r/R$, the grid spacing. Our working point for the subsequent calculations, $\triangle r/R = 0.0001$, is used as a reference to compute the relative errors (4.2).

However, for all the parameters tested, the grid spacing $\triangle r/R = 0.0001$ was shown to be fine enough to ensure that the first four digits of ω_* are independent of the grid. In the following, all results are obtained for $W/R = 10$ and $\triangle r/R = 0.0001$.

4.2. *Mode frequencies*

Figure 4 shows the dependence of ω_* on the oscillation mode n. An increase in both the angular frequency and the damping rate can be observed for growing n. This means that, when the wave length becomes smaller with respect to the radius, the membrane oscillates more frequently and dissipation acts faster. This behaviour will be discussed in more detail in section 5.

Let us now focus on the mode $n = 2$, which is the closest to an ellipse and the most used in numerical studies (Tu & Peskin, 1992; Lee & Leveque, 2003; Cottet & Maitre, 2006; Song *et al.*, 2008; Tan *et al.*, 2008), and let us investigate the dependence of ω_* on the reduced viscosity ν_*. As shown in figure 5, a decrease in ν_* leads to an increase of the real part of ω_*, and to a decrease of the absolute value of the imaginary part of ω_*. Notice that this latter tends to zero in the limit of vanishing fluid viscosity, because in the absence of any imposed membrane dissipation every damping effect disappears there.

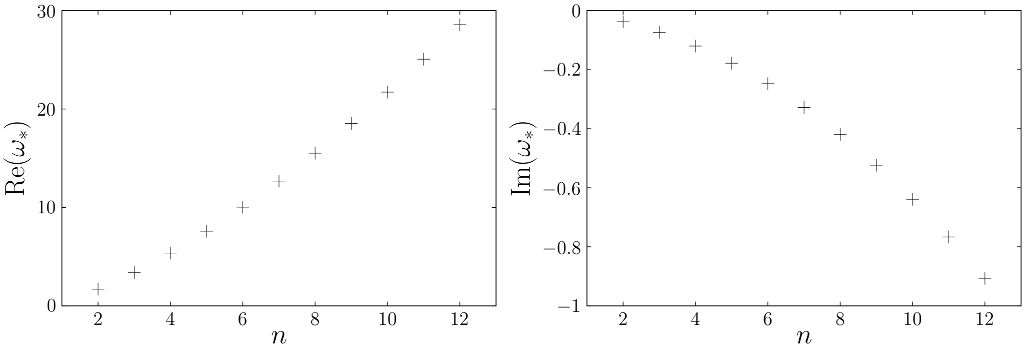

FIGURE 4. Same as in figure 2 but as a function of the oscillation mode n, for fixed values of $\nu_* = 0.001$ and $R_* = 0.5$. The modes $n = 0$ and $n = \pm 1$ must be neglected because they would imply an angle-independent evolution and a translation of the centre of mass, respectively.

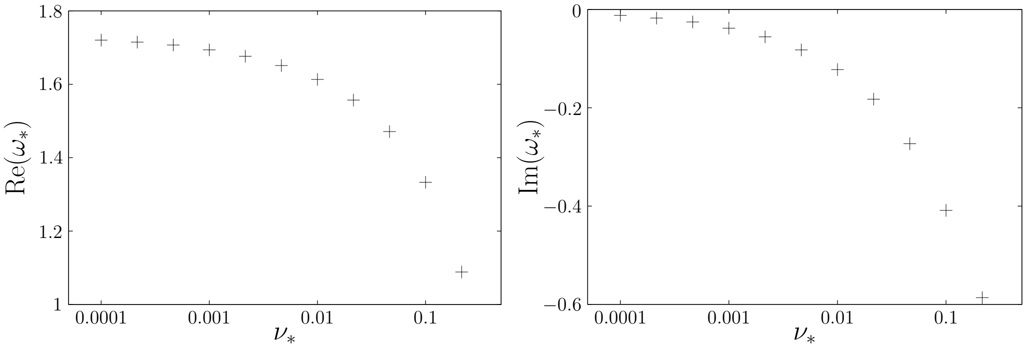

FIGURE 5. Same as in figure 2 but as a function of the reduced viscosity $\nu_* = \nu T/R^2$, for fixed values of $n = 2$ and $R_* = 0.5$.

For what concerns the dependence of ω_* on the remaining parameter R_*, we found that it is very weak, which is shown in table 1. This is due to the fact that the core of the dependence of ω on R and R_0 has already been taken into account through the definitions of the membrane time scale T and of the reduced viscosity (2.15–2.16), where the block $E(R - R_0)/R_0$ can be identified as a surface tension. Consequently, the dependence on R_* has disappeared in (3.11) and (3.13), and only lies in the jump of the second derivative (3.12).

Notice that the aforementioned dependences on n, ν_* and R_* make it impossible to find two (or more) distinct situations, namely with different oscillations modes, such as

R_*	ω_* ($\nu_* = 0.001$)	ω_* ($\nu_* = 0.05$)
0.0001	$1.693 - 0.038\mathrm{i}$	$1.457 - 0.254\mathrm{i}$
0.01	$1.693 - 0.038\mathrm{i}$	$1.457 - 0.254\mathrm{i}$
0.5	$1.693 - 0.038\mathrm{i}$	$1.457 - 0.254\mathrm{i}$
0.99	$1.693 - 0.038\mathrm{i}$	$1.460 - 0.253\mathrm{i}$
0.9999	$1.693 - 0.038\mathrm{i}$	$1.460 - 0.253\mathrm{i}$

TABLE 1. Effect of the ratio $R_* = R_0/R$ on the complex frequency ω_*, for $\nu_* = 0.001$ and $\nu_* = 0.05$ and a fixed value of $n = 2$. Only the first four digits are shown, in accordance with the results of the grid convergence study.

to have the same complex ω_*. This is due to the monotonically-growing character of both h and $|g|$ in n, which — taking into account the marginal role played by R_* — cannot be compensated by a variation in ν_*, as e.g. a reduction of the latter would imply a decrease in $\mathrm{Re}(\omega_*)$ but an increase in $|\mathrm{Im}(\omega_*)|$. However, this conclusion is no longer true for the dimensional complex ω, which can be given the same value in different modes by appropriately tuning the other parameters.

4.3. *Spatial structure of modes*

After numerically finding $\phi(r_*)$, it is possible to reconstruct the whole stream function $\psi(r, \theta, t)$ from (3.3) and thus the fluid velocity field. From the normal-mode decomposition (3.4) of $\Delta(\theta, t)$ and the following discussion, the membrane deformation is actually composed by a superposition of modes giving rise to a stationary wave (see appendix B). The mode $n = 2$ reproduces e.g. the fact that the absolute value of the membrane displacement is maximum on the axes (antinodes at $\theta = 0, \pi/2, \ldots$) and zero on the bisectors (nodes at $\theta = \pi/4, 3\pi/4, \ldots$). Instantaneous sketches of the fluid velocity in an area around the membrane are presented in figures 6–7 for three situations: our reference case, a case with different n, and a case with increased ν_* (see the values of the parameters in table 2).

Figure 6 corresponds to the passage of the membrane through the circular state, $\Delta(\theta, t) = 0$. It consists in an instantaneous capture of the fluid flow at time $t = (3\pi/2 - \sigma_\xi)/\mathrm{Re}(\omega_n)$, where the phase shift $\sigma_\xi = \arctan[-\mathrm{Im}(\xi_n)/\mathrm{Re}(\xi_n)]$ is related to the lack of the initial-value problem and its numerical value is reported in table 2. The azimuthal structure of the modes generates vortex-like motions, parts of the membrane moving outward and others inward. Note that, for $n = 3$, the flow field is more quiescent at the centre of the capsule than for $n = 2$. Changes in the flow field when increasing ν_* are less obvious, though smaller radial gradients of the azimuthal velocity for $\theta = \pi/4, 3\pi/4, \ldots$ can be seen comparing case #2 to case #0.

Figure 7 represents a time instant in the oscillation period where the membrane deformation with respect to the reference circle is maximal. More precisely, it corresponds to the first instant when the deformation is maximum and the membrane velocity vanishes, $\partial\Delta(\theta, t)/\partial t = 0$, after the time instant shown in figure 6. Indeed, here $t = (2\pi - \sigma_\phi(R))/\mathrm{Re}(\omega_n)$, where the phase shift $\sigma_\phi(R) = \arctan[-\mathrm{Im}(\phi_n(r))/\mathrm{Re}(\phi_n(r))]|_{r=R}$ is due to the absence of any initial-value imposition, and its numerical value is reported in table 2. About this state of maximum deformation, it is interesting to notice that in our formalism all the membrane points are at rest, but the fluid inertia — due to the time derivative in (2.3–2.4) — acts so as to maintain some fluid motion almost everywhere at any time, as noticeable in figure 7. In particular, high azimuthal velocity is observed just outside the membrane for $\theta = \pi/2n, 3\pi/2n, \ldots$. Note that the thickness of the layer where velocity is not null grows with ν_*.

As a comparison, we also provide results from numerical simulations, obtained via the in-house YALES2BIO solver developed at Institut de Mathématiques et de Modé-

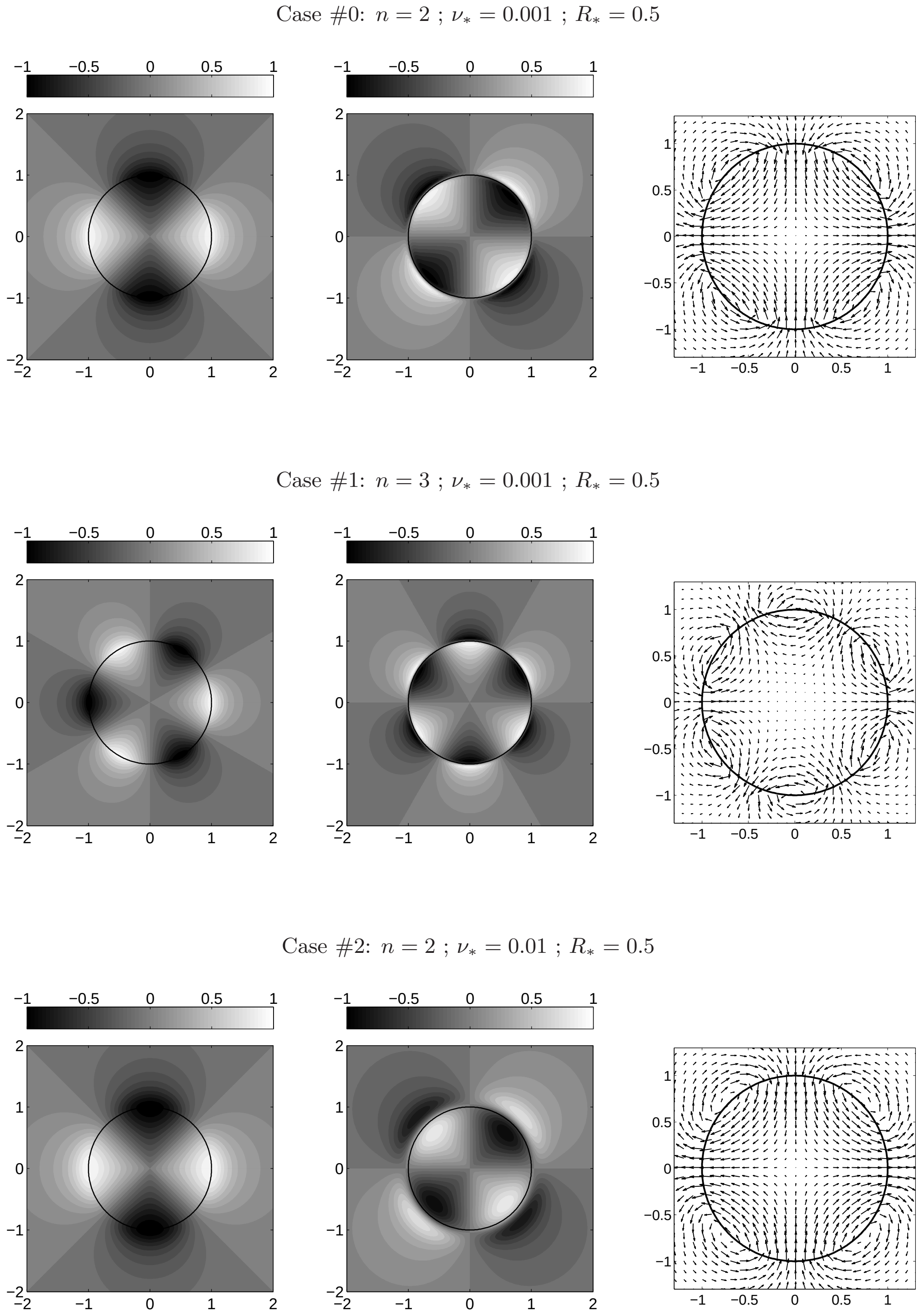
Case #0: $n = 2$; $\nu_* = 0.001$; $R_* = 0.5$

Case #1: $n = 3$; $\nu_* = 0.001$; $R_* = 0.5$

Case #2: $n = 2$; $\nu_* = 0.01$; $R_* = 0.5$

FIGURE 6. Normalised fluid velocity in an area around the membrane, captured at a passage time of the membrane through the reference circle (represented by the black line). From table 2, plotted are the "standard" case #0 (top), case #1 with different n (middle), and case #2 with increased ν_* (bottom). Left panels represent the radial component, centre panels the azimuthal component and right panels display velocity vectors over a smaller domain. Notice that u_θ is continuous according to (2.13), but it varies very rapidly across the membrane at the angle $\theta = \pi/2n$ and odd multiples. The arrows denote the direction of the local instantaneous membrane motion and are conventionally placed at the angle $\theta = \pi/n$ and multiples, where

Case #0: $n = 2$; $\nu_* = 0.001$; $R_* = 0.5$

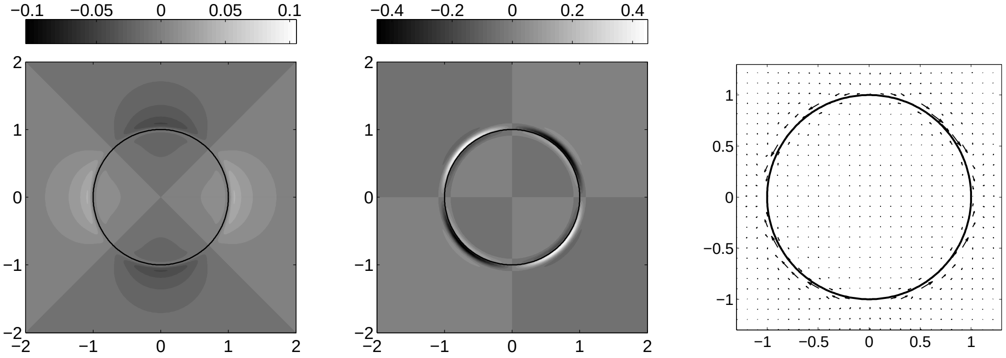

Case #1: $n = 3$; $\nu_* = 0.001$; $R_* = 0.5$

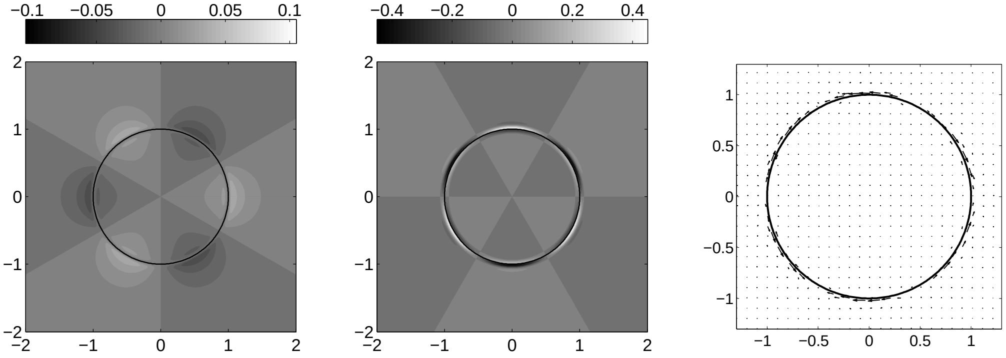

Case #2: $n = 2$; $\nu_* = 0.01$; $R_* = 0.5$

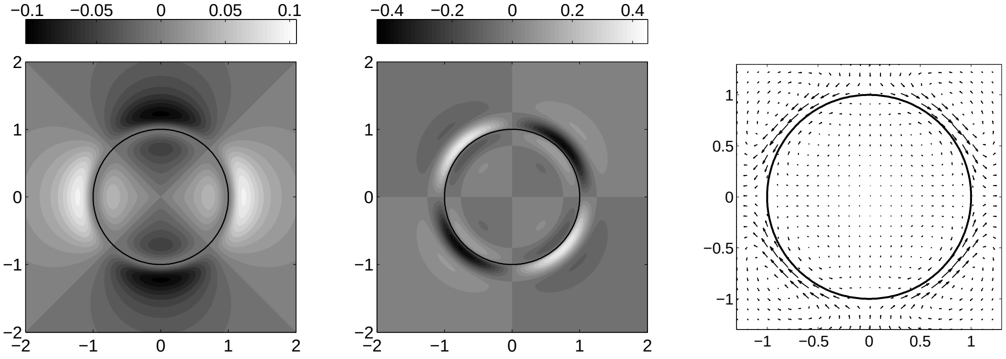

FIGURE 7. Same as in figure 6, but captured at a time of maximum deformation when the whole membrane is at rest. The time instant is chosen to be the one following the capture time of figure 6, i.e. slightly less than one fourth of a period later. As the normalization of both velocity components with the same above-defined U — the maximum speed value reached during the passage through the circle in figure 6 — is maintained, notice the orders of magnitude: small for the azimuthal component and even smaller for the radial one. Also note that the black line represents the reference circle, and not the actual present position of the membrane.

case	n	ν_*	R_*	ω_* (analytical)	ω_* (numerical)	σ_ξ	$\sigma_\phi(R)$
#0	2	0.001	0.5	1.693 − 0.038i	1.670 − 0.040i	−0.0184	0.00495
#1	3	0.001	0.5	3.395 − 0.071i	3.335 − 0.067i	−0.0209	0.00249
#2	2	0.01	0.5	1.615 − 0.122i	1.577 − 0.143i	−0.0578	0.0179

Table 2. The set of parameters, n, ν_* and R_*, used for the three situations represented in each row of figures 6–8, and indicated by different grey filling tones in figure 11. Case #0 is the reference benchmark. Also reported are the values of the nondimensional complex angular frequency ω_*, from the present linear analysis and from YALES2BIO simulations (see text); and the values of the phase shifts, σ_ξ and $\sigma_\phi(R)$, which dictate the time instants at which figures 6&8 and figure 7 are captured, respectively (see (B 4) and (B 7)).

lisation de Montpellier (http://www.math.univ-montp2.fr/∼yales2bio/). YALES2BIO builds heavily upon the YALES2 solver (http://www.coria-cfd.fr/index.php/YALES2) designed at the CORIA (CNRS UMR 6614), which solves the incompressible Navier–Stokes equations using a finite-volume approach (Moureau *et al.*, 2011*a*,*b*). The classical immersed-boundary method, or IBM (Peskin, 1977), is implemented to solve the present fluid–structure interaction problem. The numerical method and its extensive validation are presented by Mendez, Gibaud & Nicoud (2014). The capsule is represented as a set of discrete massless markers convected by the flow field, and pairwise connected by straight-line springs, as in the original IBM by Peskin (1977). Given the strain in each spring, the state of membrane stress is obtained, and the information is passed to the fluid-flow solver, which solves the Navier–Stokes equations forced by the membrane action. Thanks to the ability of the solver to use hybrid fluid grids, the fluid mesh is composed by two zones: one with regular square cells in the membrane neighbourhood and one with triangular cells, far from the membrane. This enables us to limit the number of grid points by coarsening the grid far from the region of interest. In the Cartesian region fluid-structure coupling is realized using the classical regularization/interpolation operator for regular grids, based on a cosine function (Peskin, 1977). A grid convergence study has been led to present grid-independent results. In the reported calculations, the membrane is discretised with 2500 markers, while in the near-membrane region the fluid grid resolution is of the order of $2\pi R/2500$. As already stated in the introduction, IBM and similar methods have often been used to simulate the damped oscillations of an initially-elliptic capsule (Tu & Peskin, 1992; Lee & Leveque, 2003; Song *et al.*, 2008; Tan *et al.*, 2008). Circular capsules are initially deformed with a small perturbation (to allow for the comparison with the analytical approach) of given azimuthal wave number, and plugged in a fluid at rest. The capsule is let evolve and oscillates before reaching the circular equilibrium shape. The frequency and damping rate of oscillations are extracted from the temporal evolution of the markers' position. First periods are not considered, in order not to spoil the results with effects of the initial conditions. It is important to stress that, in these computations, the full Navier–Stokes equations are solved and the membrane actually oscillates around the equilibrium shape. The full non-linear problem (fluid and membrane) is addressed in the YALES2BIO simulations.

Values of the angular frequency ω_* are displayed in table 2. Figure 8 displays the dependence of the velocity field on the radial variable, for both the radial and the azimuthal component, in the three situations already mentioned and at a passage time through the circle (corresponding to figure 6). First, the comparison between the full numerical approach and the small-perturbation analysis developed in this paper shows the quality of the results. Excellent agreement is obtained between the two completely different approaches. Note that YALES2BIO solves the full Navier-Stokes equations, including the non-linear term. The agreement of the results with the present analysis, which starts from the unsteady Stokes equations, confirms that the non-linear term is unimportant in the cases considered. Figure 8 enables to quantify effects already visible in figure 6. In particular, it shows how the velocity decreases more rapidly away from the membrane when n increases. A comparison between the first and last row show that, by increasing viscosity, velocity gradients decrease and azimuthal velocity extrema are reached further away from the membrane. The right panels also display the radial derivative of u_θ, whose jump makes $\partial u_\theta/\partial r_*$ reach higher values outside the capsule than inside over a layer whose size increases with ν_*.

5. Discussion

In this section we compare our results to similar cases already studied in the literature, and we propose a physical model to interpret them.

5.1. *Droplets*

A first comparison can be carried out with the case of droplet oscillations. Kelvin (1890) and Rayleigh (1896) analysed this problem in the presence of a three-dimensional inviscid/potential/irrotational flow, for which no damping occurs, in the specific cases of cavities or gas bubbles in a liquid or of liquid drops in vacuum. Lamb (1932); Chandrasekhar (1961); Miller & Scriven (1968) and Padrino *et al.* (2008) later removed these limitations successively. Prosperetti (1980*b*) noticed the presence of a full continuous spectrum of complex frequencies — namely, purely-imaginary ones, corresponding to a pure damping — besides the classical "isolated" solution in the complex plane. Even if the latter is the only relevant to us, because endowed with non-zero real and imaginary parts, through our numerical procedure to solve (3.11–3.13) we also find a hint of the existence of a set of several imaginary solutions, which is probably not continuous due to the presence of the external wall but which confirms the agreement with the litera-

Case #0: $n = 2$; $\nu_* = 0.001$; $R_* = 0.5$

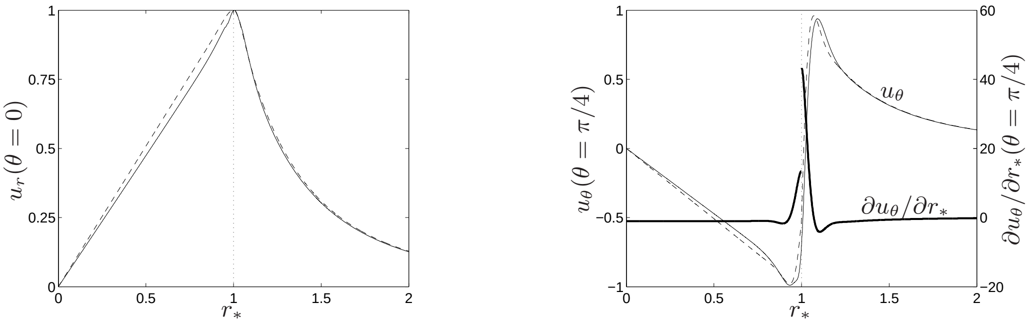

Case #1: $n = 3$; $\nu_* = 0.001$; $R_* = 0.5$

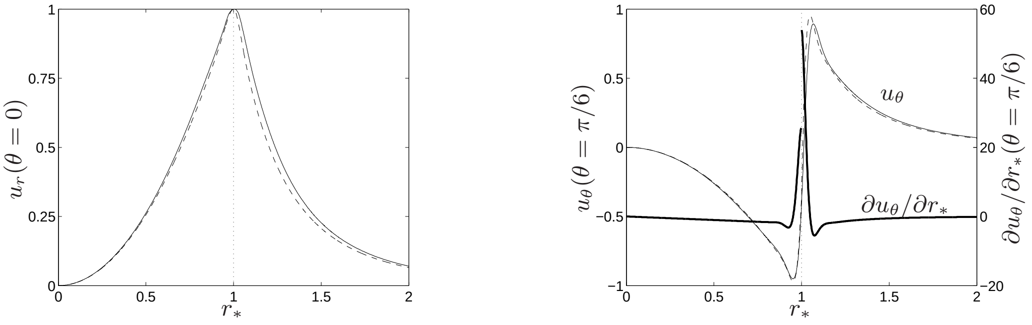

Case #2: $n = 2$; $\nu_* = 0.01$; $R_* = 0.5$

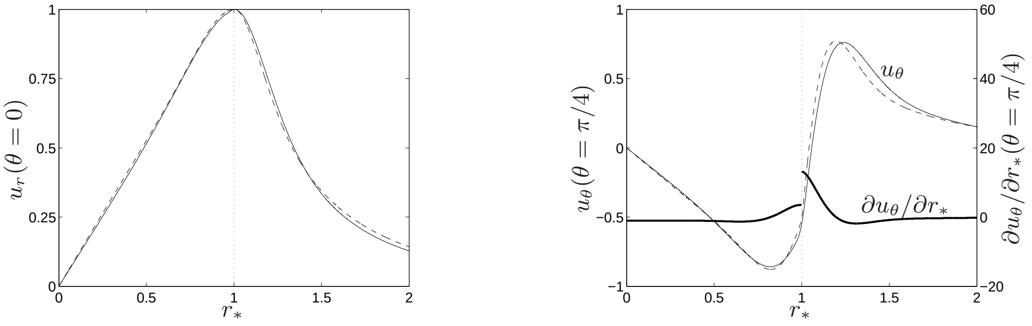

FIGURE 8. Radial dependence of one component of the fluid velocity, captured at one passage time of the membrane through the reference circle, from the analytical approach (----) and from numerical simulations (—). The location of the membrane is shown with a vertical dotted line. Left panels show the radial velocity at $\theta = 0$ (where u_θ is analytically zero), right panels show the azimuthal velocity at $\theta = \pi/2n$ (where u_r is analytically zero). The radial derivative of u_θ obtained with the analytical approach is superimposed on the right panels (━). Plotted are the three cases of table 2.

ture even for a different situation. Prosperetti (1980*a*) also analysed the oscillations of bubbles and drops in terms of the initial-value problem, which as already stated is not our aim here. Theoretical and experimental results on the role of surfactants were found by Lu & Apfel (1991) and Abi Chebel *et al.* (2012). Surfactant-coated bubbles were also investigated in Kropinski & Lushi (2011).

From the aforementioned references, a general expression for the oscillation angular frequency in 3-D inviscid flows is

$$\mathrm{Re}(\omega) = \left\{ \frac{(n-1)n(n+1)(n+2)\zeta}{R^3[n\rho_{\mathrm{ext}} + (n+1)\rho_{\mathrm{int}}]} \right\}^{1/2} , \tag{5.1}$$

while for 2-D one gets

$$\mathrm{Re}(\omega) = \left[\frac{(n-1)n(n+1)\zeta}{R^3(\rho_{\mathrm{ext}} + \rho_{\mathrm{int}})} \right]^{1/2} , \tag{5.2}$$

There, ζ is the surface tension (equivalent to our $E(R-R_0)/R_0$), and the fluids external and internal to the membrane may have any mass densities (ρ_{ext} and ρ_{int}, respectively). Therefore, in our notation, (5.2) becomes:

$$\mathrm{Re}(\omega_*) = \sqrt{\frac{(n-1)n(n+1)}{2}} . \tag{5.3}$$

Cumbersome formulae also exist in literature (Lamb, 1932; Miller & Scriven, 1968) for the damping rate $\mathrm{Im}(\omega)$ of droplets or bubbles, or for fluids of very high or low viscosities. In our formalism, a droplet (in another liquid of the same density) can be thought of as a membrane with uniform surface tension, which amounts to neglecting the angle-dependent term in (2.9) (and thus to pose $\chi = \bar{\chi}$ in (2.10)). As a consequence, equation (3.11) and constraint (3.13) keep the same form, but the interfacial jump of the second derivative is now given no longer by (3.12) but rather by:

$$\phi^{(2)-} - \phi^{(2)+} = 0 . \tag{5.4}$$

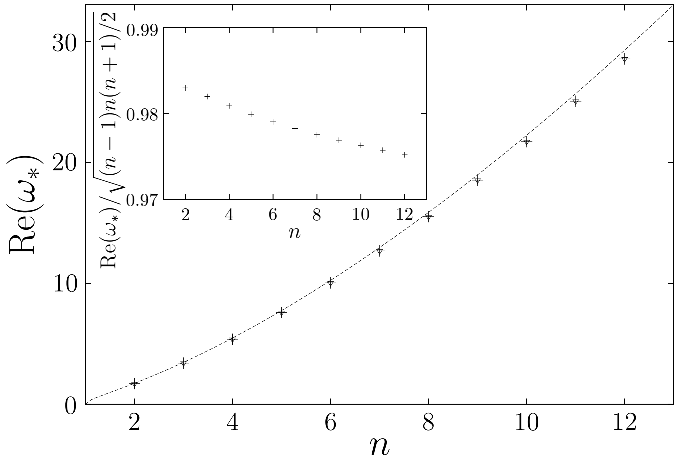

FIGURE 9. Same as in the left panel of figure 2 but with the imposition of constraint (5.4) for droplets (+). For comparison, also the case of membranes with the usual constraint (3.12) is plotted (▽). (The difference is almost undistinguishable on this scale, but for the modes $n = 2, 3$ a small discrepancy can be noticed from the forthcoming figure 11.) The dashed line represents the inviscid prediction from (5.3) which turns out to be accurate, as confirmed by the fact that the ratio plotted in the insert approximately equals 1. The reduced viscosity is $\nu_* = 0.001$.

In figure 9 we show the (real part of) the angular frequency as a function of n if constraint (5.4) is imposed, together with the inviscid prediction from (5.3). The reduced viscosity is $\nu_* = 0.001$. The ratio $\mathrm{Re}(\omega_*)/[(n-1)n(n+1)/2]^{1/2}$, depicted in the insert of figure 9, is shown to be almost constant ($\simeq 1$), which proves that prediction (5.3) is excellent.

5.2. *Radial transport*

It is also interesting to investigate what happens when the membrane can slip with respect to the fluid, and the latter transports the former only in the radial direction. In this case, the appropriate expression for the elongation is no more the dynamical one (2.9) but rather a purely-geometric one

$$\chi(\theta,t) = \frac{\mathcal{R}(\theta,t) - R_0}{R_0} = \frac{R - R_0}{R_0} + \frac{\Delta(\theta,t)}{R_0} \ , \tag{5.5}$$

which does not make the fluid velocity appear explicitly — differently from (2.12). The consequence of this modification in the forcing terms (2.5) is once again encoded in a change of the second-derivative jump, from (3.12) to

$$\phi^{(2)-} - \phi^{(2)+} = \frac{\mathrm{i}n^2}{\omega_* \nu_* (1 - R_*)} \phi(1) \; , \tag{5.6}$$

while (3.11) and (3.13) maintain the same form. (The consequent results will be described in figure 10.) We can assert that, with respect to a purely-radial slippery transport, the mechanism of tangential friction and transport increases the degree of homogenization of the membrane elongation or tension, towards the limiting case of perfect homogenization represented by droplets.

We can now propose a physical model to interpret our results, based on the concepts of entrained fluid and vibrating string. Keeping somehow in mind the phenomenology of fluid–structure interaction problems, we can think that the membrane entrains some fluid during its movement, because mass conservation (or, equivalently, the impossibility of creating vacuum pockets) forces some fluid to follow the membrane in its radial movement. This explains why oscillations can be observed. Indeed, a deformed massless membrane in vacuum would asymptotically (i.e., with a vanishing final velocity) reach its equilibrium shape without overpassing it, and the same would hold in a fluid described by the pure Stokes equation. However, even in the absence of the non-linear advective contribution from the full Navier–Stokes equation, the presence of the time derivative represents a fluid inertial term which justifies the observed multiple overpassing. The effective inertia of the membrane can thus be quantified by investigating how much fluid is carried per unit membrane surface (here, length), i.e. by finding its equivalent thickness. It is well known that a rectilinear open string under vibration has oscillation angular frequency Ω and tension (per unit length in the third invariant direction z, perpendicular to the oscillation plane) $\mathcal{T}$ given by

$$\Omega = \frac{n}{R}\sqrt{\frac{\mathcal{T}}{\mathcal{M}}} \, , \qquad \mathcal{T} = E\bar{\chi} \, , \tag{5.7}$$

where $\mathcal{M}$ is the mass per unit string arclength and per unit length in z. Now, this would usually be given by the mass of a solid material string in vacuum; but here the key point is that, due to the massless membrane, this mass is exclusively represented by the fluid, so we can express it in terms of an equivalent fluid thickness d as:

$$\mathcal{M} = \rho d \, . \tag{5.8}$$

Inverting (5.8), exploiting (5.7) and keeping into account that $\bar{\chi} = E(R - R_0)/R_0$ for a quasi-circular membrane, we obtain:

$$d = \frac{\mathcal{M}}{\rho} = \frac{E}{\rho}\frac{R - R_0}{R_0}\left(\frac{n}{R\Omega}\right)^2 \, . \tag{5.9}$$

Equation (5.9) allows us to empirically find an effective thickness for each case we simulate numerically, by substituting the outcome $\mathrm{Re}(\omega)$ in place of Ω. For the cases of purely-radial transport (5.6), our guess is an approximately linear relation between d and the wavelength $\lambda = 2\pi R/n$. Indeed, if one defines this proportionality factor as $\alpha = d/\lambda$, replacing this empirical relation into (5.9) and nondimensionalising, one gets

$$\mathrm{Re}(\omega_*) = \sqrt{\frac{n^3}{2\pi\alpha}} = \beta n^{3/2} \, , \tag{5.10}$$

where $\beta = (2\pi\alpha)^{-1/2}$. The insert of figure 10 shows that our scheme predicts that the limiting value of $\mathrm{Re}(\omega_*)/n^{3/2}$ is $\beta \simeq 0.7$, and such a value is used in figure 10 to reproduce the fit (5.10). As a consequence, $d/\lambda = \alpha = 1/2\pi\beta^2 \simeq 0.3$.

Here, two comments are in order. First, such an approximation looks weaker at very small n. Our explanation lies in the observation that (5.7) is valid for a rectilinear open string, for which there is an exact symmetry between "up" and "down". For our circular closed membrane, this is approximately true for a sufficiently large n, where the wave

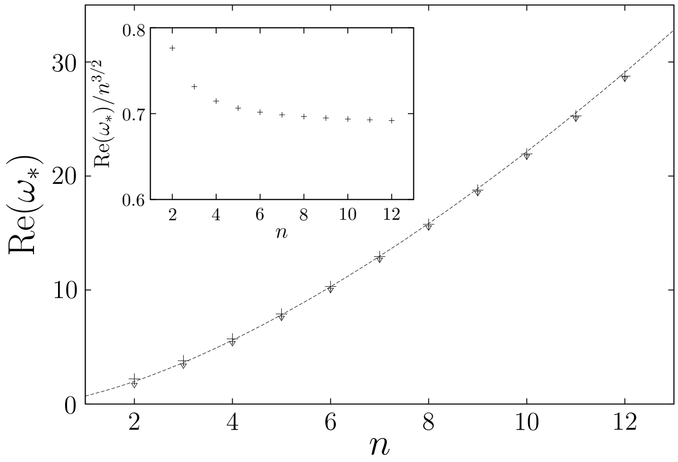

FIGURE 10. Same as in the left panel of figure 2 but with the imposition of constraint (5.6) for radial transport (+). For comparison, also the case of complete transport with the usual constraint (3.12) is plotted (▽). (The difference is very small on this scale, but for the modes $n = 2, 3$ a definite discrepancy can be noticed from the forthcoming figure 11.) The dashed line represents the prediction from our model (5.10), where the coefficient $\beta = 0.7$ has been fitted from the ratio plotted in the insert. The reduced viscosity is $\nu_* = 0.001$.

length is smaller than the radius, but clearly not for small n because there curvature effects become relevant and a net asymmetry arises between "inside" and "outside". Secondly, for the general case of complete transport (3.12), the value of β tends to $\simeq 0.7$ from below — rather than from above — at large n, so one may think that in this latter asymptotics the slippery and complete cases tend to coincide.

5.3. *Comparison between different schemes*

The results for ω_* corresponding to imposing (3.12) — with its numerical counterpart from YALES2BIO — or (5.4) or (5.6) are plotted in figure 11, for three sets of parameters: our reference case, a case with different n, and a case with increased ν_*. The full CFD approach turns out to be in excellent agreement with the present analytical point of view. From the larger spreading of the grey symbols we deduce that, when the reduced viscosity is higher, the role of the interface conditions is more relevant, in the sense that

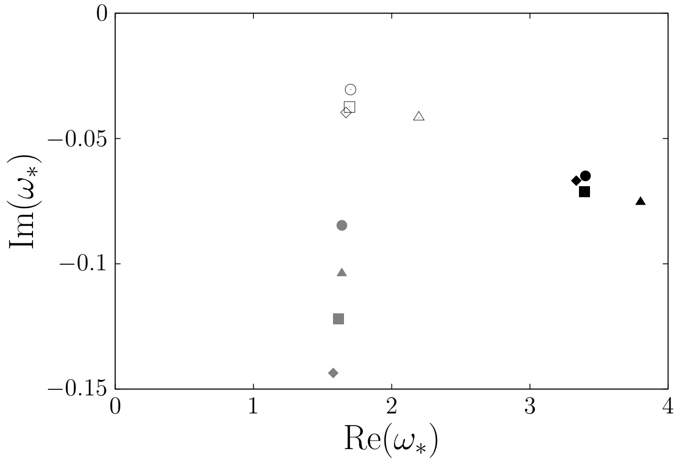

FIGURE 11. Location of the solutions in the complex ω_* plane for the reference case #0 (open symbols), together with cases #1 (filled symbols) and #2 (grey symbols). Squares represent the usual calculations with constraint (3.12), and diamonds their numerical counterparts from YALES2BIO; circles represent droplets (constraint (5.4)); triangles represent purely-radial transport with slippery membrane (constraint (5.6)).

the cases of droplets and of purely-radial transport become definitely separated from the original capsule one. On the contrary, filled symbols are as spread out as open ones, which means that the importance of the interface conditions does not change when increasing the mode index from 2 to 3.

In particular, it is interesting to investigate the ratio between the (absolute value of the) imaginary part and the real one, and its behaviour with the reduced viscosity. Figure 12 shows that a power law with exponent 0.55 and unit prefactor is an excellent approximation of all three schemes — membrane, droplet and radial transport. This implies that, once an effective inverse time scale is introduced as a reference unit via $\mathrm{Re}(\omega)$ and/or expressions (5.3,5.10), the damping rate in this unit is of course a growing function of ν_*, but is almost independent of the implemented physical scheme. In other words, at fixed reduced viscosity, the effects of the interfacial boundary layer look negligible to compute $\mathrm{Im}(\omega_*)$ in the aforementioned rescaled unit.

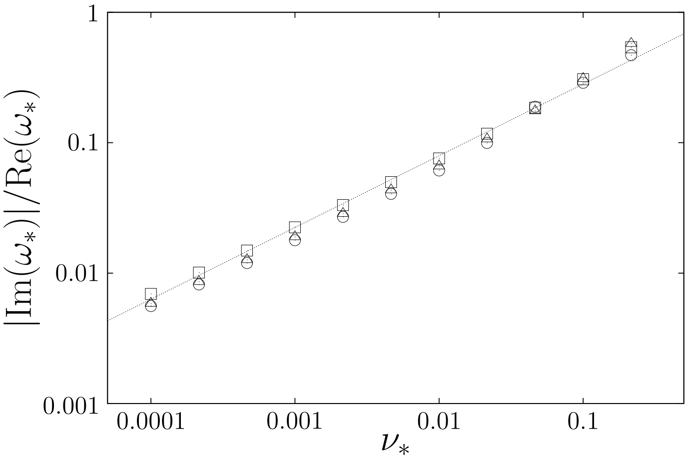

FIGURE 12. Ratio between the (opposite of the) imaginary part and the real part of the complex frequency plotted in figure 5. Squares, circles and triangles have the same meaning as in figure 11, while the dashed line represents the fit $|\mathrm{Im}(\omega_*)|/\mathrm{Re}(\omega_*) = \nu_*^{0.55}$.

6. Conclusions and perspectives

We have investigated the damped oscillations of a massless elastic membrane immersed in a two-dimensional viscous incompressible fluid. By introducing a normal-mode decomposition of the stream function, we have analytically obtained a fourth-order linear ordinary differential equation. Such an equation possesses non-trivial solutions only for a subset of complex frequencies, and namely for a unique value of ω with non-zero both real (oscillation angular frequency) and imaginary (damping rate) parts. By means of an appropriate nondimensionalisation of the problem, the latter two quantities have been shown to depend on the oscillation mode, on the reduced viscosity and on the pre-inflation ratio. A detailed numerical study of these behaviours has been performed, as well as an (excellent) comparison with the results of a fully-computational procedure we have developed using the YALES2BIO code, in terms of both the complex-valued eigenvalues ω and the corresponding eigenvectors — i.e. the spatial structure of the induced fluid flow.

An interesting feature of our approach is that it unifies the case of an elastic capsule with those of a droplet or of a slippery membrane, in the sense that simply turning on or off some parameters in the equations we have been able to reproduce the corresponding results from the scientific literature or from the simple physical model we have proposed.

The present work is also the first, to the best knowledge of its authors, to provide semi-analytical results in the case of damped oscillations of a two-dimensional capsule closed by an elastic membrane, though it has proven to be a popular configuration in quality assessment of numerical methods for computing the dynamics of capsules. It is anticipated that our results could be used as a quantitative validation for future numerical methods.

Among the perspectives, we would like to mention the possibility of introducing an external shear flow or a background velocity around the membrane, rather than the presence of a circular solid wall. Also, it would be interesting to consider small perturbations of non-circular geometries, especially in the presence of inextensible membranes (Veerapaneni *et al.*, 2011). Finally, in the framework of fluid–structure interaction and energy harvesting, a connection possibly arises with the study of 2-D hinged flapping filaments (**??**), where spontaneous symmetry-breaking in the oscillations induces non-trivial effects on drag and lift.

We thank Etienne Gibaud, Vanessa Lleras, Daniele di Pietro, Matthieu Alfaro and Rémi Carles for useful discussions and suggestions. We acknowledge financial support from LabEx NUMEV (ANR-10-LABX-20), ANR FORCE (ANR-11-JS09-0011) and Dat@Diag (OSEO).

Appendix A. Local instantaneous elongation of the membrane

The membrane elongation is defined as

$$\chi(\theta,t)=\frac{L(\theta,t)-L_0}{L_0}\ . \tag{A 1}$$

letter	definition	description
$\mathtt{A}$		matrix in appendix C
a, b, c		Boolean indicators in appendix C
d		equivalent fluid thickness for vibrating string
E		membrane thickness times Young modulus (constant)
$\hat{e}_r$		radial unit vector
$\hat{e}_\theta$		azimuthal unit vector
$\mathcal{E}_{\mathrm{Re}}$		relative error for real part in grid convergence (4.2)
$\mathcal{E}_{\mathrm{Im}}$		relative error for imaginary part in grid convergence
$\boldsymbol{f}(r,\theta,t)$		line force per unit volume exerted by membrane on fluid
$f_r(r,\theta,t)$		radial component of $\boldsymbol{f}$
$f_\theta(r,\theta,t)$		azimuthal component of $\boldsymbol{f}$
$g(n,\nu_*,R_*)$	$\mathrm{Im}(\omega_*)$	damping rate of membrane oscillation
$h(n,\nu_*,R_*)$	$\mathrm{Re}(\omega_*)$	angular frequency of membrane oscillation
K	$k-1$	
k		matrix row index in appendix C
$L(\theta,t)$		local instantaneous length of infinitesimal membrane arc
L_0		constant value of L in deflated state
M		number of total discretisation points in radial direction
m		number of discretisation points in internal region
$\mathcal{M}$		mass (per unit arclength and z) of vibrating string
$\hat{\boldsymbol{N}}$		unit vector inward normal to membrane
n		oscillation mode index
$p(r,\theta,t)$		fluid pressure
q	$\triangle r/R$	
R		radius of reference circle (inflated membrane at rest)
R_0		radius of the unstressed circular membrane
R_*	R_0/R	inverse of inflation ratio
$\boldsymbol{r}$		space variable
r		radial coordinate
r_*	r/R	nondimensionalised radial coordinate
$\mathcal{R}(\theta,t)$		local instantaneous membrane location
s		curvilinear abscissa
T	$\sqrt{\rho R^3 R_0/E(R-R_0)}$	membrane characteristic time
t		time variable

symbol	definition	description
α	d/λ	
β	$1/\sqrt{2\pi\alpha}$	
$\Gamma(\theta, t)$		local instantaneous membrane curvature
γ_n, γ		amplitude of $\tilde{\chi}$ in mode n
$\Delta(\theta, t)$	$\mathcal{R}(\theta, t) - R$	local instantaneous membrane departure from circle
$\triangle r$	$W/(M-1)$	grid spacing in the radial direction
θ		azimuthal angle
λ	$2\pi R/n$	wavelength
μ	$\rho\nu$	constant fluid dynamic viscosity
ν		constant fluid kinematic viscosity
ν_*	$\nu T/R^2$	reduced viscosity
ρ		constant fluid mass density
$\sigma_\phi(r)$	$\arctan[-\mathrm{Im}(\phi)/\mathrm{Re}(\phi)]\|_r$	phase shift of stream function amplitude
σ_ξ	$\arctan[-\mathrm{Im}(\xi)/\mathrm{Re}(\xi)]$	phase shift of membrane excess radius amplitude
σ_ω	$\arctan[-\mathrm{Im}(\omega)/\mathrm{Re}(\omega)]$	phase shift of complex angular frequency
$\hat{\boldsymbol{\tau}}$		unit vector counterclockwise tangential to membrane
$\phi_n(r)$, $\phi(r)$		amplitude of ψ in mode n
$\chi(\theta, t)$		local instantaneous membrane elongation
$\bar{\chi}$		constant mean membrane elongation (averaged on θ)
$\tilde{\chi}(\theta, t)$		local instantaneous fluctuation of membrane elongation
$\psi(r, \theta, t)$		fluid stream function
ξ_n, ξ		amplitude of Δ in mode n
Ω		oscillation angular frequency of vibrating string
ω_n, ω		complex angular frequency in mode n
ω_*	ωT	nondimensionalised complex angular frequency
$_{\mathrm{ext}}$		relative to external fluid
$_{\mathrm{int}}$		relative to internal fluid
$^{\mathrm{WP}}$		computed at working point $\triangle r/R = 0.0001$
$'$	$\partial/\partial\theta$	angular derivative
$\dot{}$		derivative with respect to argument
$^{(l)}$	$\partial^l/\partial r^l$	l-th order radial derivative
$^{+}$	$\lim_{r\to R_+}$	limit of fluid quantity at interface from exterior
$^{-}$	$\lim_{r\to R_-}$	limit of fluid quantity at interface from interior

To describe the membrane elongation, let us consider a material element of length $L(t) = ||\boldsymbol{x} - \boldsymbol{x}_\dagger|| = \mathrm{d}s$, between a point $\boldsymbol{x} = (R + \Delta(\theta, t), \theta)$ (in polar coordinates) and its neighbour $\boldsymbol{x}_\dagger = \boldsymbol{x} + \hat{\boldsymbol{\tau}}\mathrm{d}s$. After an infinitesimal time $\mathrm{d}t$, these two points are located in $\boldsymbol{x}^\star = \boldsymbol{x} + \boldsymbol{u}(\boldsymbol{x}, t)\mathrm{d}t$ and $\boldsymbol{x}^\star_\dagger = \boldsymbol{x}_\dagger + [\boldsymbol{u}(\boldsymbol{x}, t) + (\boldsymbol{x}_\dagger - \boldsymbol{x}) \cdot \nabla\boldsymbol{u}(\boldsymbol{x}, t)]\mathrm{d}t$, respectively, from which one can easily obtain the new length $L(t + \mathrm{d}t)$. Using $\hat{\boldsymbol{\tau}} = [(R + \Delta)^2 + \Delta'^2]^{-1/2}\,[\Delta'\hat{\boldsymbol{e}}_r + (R + \Delta)\hat{\boldsymbol{e}}_\theta]$, after straightforward algebra, the length increment reads

$$L(t+\mathrm{d}t) - L(t) = \mathrm{d}t\,\mathrm{d}s\left[\frac{\Delta'\dfrac{\mathrm{d}u_r}{\mathrm{d}\tau} + (R+\Delta)\dfrac{\mathrm{d}u_\theta}{\mathrm{d}\tau}}{\sqrt{(R+\Delta)^2 + \Delta'^2}} + \frac{(R+\Delta)u_r - \Delta' u_\theta}{(R+\Delta)^2 + \Delta'^2}\right] , \qquad (\mathrm{A}\,2)$$

where all velocities and their derivatives must be computed at $(R + \Delta(\theta, t), \theta)$. Plugging this result into (A 1) and eliminating L_0, we get:

$$\begin{aligned}\chi(t+\mathrm{d}t) - \chi(t) &= \frac{L(t+\mathrm{d}t) - L_0}{L_0} - \frac{L(t) - L_0}{L_0} = \frac{L(t+\mathrm{d}t) - L(t)}{L(t)/[\chi(t)+1]} \qquad (\mathrm{A}\,3)\\ &= \frac{\mathrm{d}t\,[\chi(t)+1]}{(R+\Delta)^2 + \Delta'^2}\left[\Delta'\left(\frac{\partial u_r}{\partial\theta} - u_\theta\right) + (R+\Delta)\left(\frac{\partial u_\theta}{\partial\theta} + u_r\right)\right].\end{aligned}$$

Replacing the membrane elongation by its decomposition into a mean part and a fluctuating part $\tilde{\chi}$ into (A 3), on the left-hand side only the fluctuating part survives, and at leading order on the right-hand side we can neglect both the fluctuating part in χ and the quadratically-small terms with Δ and Δ' (remember that, in this approach, $\boldsymbol{u}$ is a small quantity itself). For the same reason, dividing (A 3) by $\mathrm{d}t$, we can interpret the material derivative $\mathrm{d}\tilde{\chi}/\mathrm{d}t$ as a temporal partial derivative $\partial\tilde{\chi}/\partial t$, because of the quadratic smallness of the convective contribution; and we can also consider all velocities and their derivatives as computed at (R, θ). We are left with:

$$\frac{\partial\tilde{\chi}(\theta, t)}{\partial t} = \frac{\bar{\chi} + 1}{R}\left[\frac{\partial u_\theta}{\partial\theta} + u_r\right](R, \theta, t)\ . \qquad (\mathrm{A}\,4)$$

Appendix B. Details of the analytical procedure

In this appendix we show in more details the calculations leading to equation (3.6).

Plugging (3.2) into (3.1), we get:

$$\begin{aligned} r^4\frac{\partial^3\psi}{\partial r^2\partial t}+r^2\frac{\partial^3\psi}{\partial\theta^2\partial t}+r^3\frac{\partial^2\psi}{\partial r\partial t} = \nu\Bigg(& r^4\frac{\partial^4\psi}{\partial r^4}+2r^2\frac{\partial^4\psi}{\partial r^2\partial\theta^2}+\frac{\partial^4\psi}{\partial\theta^4}+2r^3\frac{\partial^3\psi}{\partial r^3} \\ & -2r\frac{\partial^3\psi}{\partial r\partial\theta^2}-r^2\frac{\partial^2\psi}{\partial r^2}+4\frac{\partial^2\psi}{\partial\theta^2}+r\frac{\partial\psi}{\partial r}\Bigg) \\ & +\frac{E}{\rho R_0}\left\{\left[\Delta'\left(1-\frac{R_0}{R}\right)\left(1-\frac{r}{R}\right)-\frac{rR_0}{R}\chi'\right]\dot\delta(r-R)\right. \\ & \left.+\left[\frac{\Delta'''}{R}\left(1-\frac{R_0}{R}\right)-2\frac{R_0}{R}\chi'\right]\delta(r-R)\right\}r^3\ . \end{aligned} \tag{B 1}$$

Equation (B 1) is accompanied by an appropriate rewriting of the continuity and boundary conditions, and can be closed thanks to two relations expressing the geometric displacement Δ and the dynamical elongation χ as functions of the fluid quantity $\psi(R)$, as we are going to show.

Substituting the normal mode decomposition of ψ, Δ and $\tilde\chi$ (3.3–3.5) into (B 1), we are left with an ordinary differential equation for ϕ for each value of n, namely a fourth-order linear homogeneous one:

$$\begin{aligned} & \phi^{(4)}+\frac{2}{r}\phi^{(3)}+\left(-\frac{2n^2+1}{r^2}+\frac{\mathrm{i}\omega}{\nu}\right)\phi^{(2)} \\ & +\left(\frac{2n^2+1}{r^3}+\frac{\mathrm{i}\omega}{\nu r}\right)\phi^{(1)}+\left(\frac{n^4-4n^2}{r^4}-\frac{\mathrm{i}\omega n^2}{\nu r^2}\right)\phi \\ & +\frac{\mathrm{i}nE}{\mu R_0}\left\{\left[\left(1-\frac{R_0}{R}\right)\left(1-\frac{r}{R}\right)\xi-\frac{rR_0}{R}\gamma\right]\dot\delta(r-R)\right. \\ & \left.-\frac{1}{R}\left[n^2\left(1-\frac{R_0}{R}\right)\xi+2R_0\gamma\right]\delta(r-R)\right\}=0\ . \end{aligned} \tag{B 2}$$

This must be supplemented with a proper reformulation of the constraints on velocity at the membrane (2.13) and of the boundary conditions (2.14) in terms of the stream function and then of ϕ. The boundary conditions at the origin and at the (circular) wall now read

$$\begin{aligned} \left.\frac{\phi}{r}\mathrm{i}n\mathrm{e}^{\mathrm{i}(n\theta-\omega t)}\right|_{r=0} &= 0 = \left.\left(\frac{\phi^{(1)}}{r}-\frac{\phi}{r^2}\right)\mathrm{i}n\mathrm{e}^{\mathrm{i}(n\theta-\omega t)}\right|_{r=0}\ , \\ \left.\frac{\phi}{r}\mathrm{i}n\mathrm{e}^{\mathrm{i}(n\theta-\omega t)}\right|_{r=W} &= 0 = \left.-\phi^{(1)}\mathrm{e}^{\mathrm{i}(n\theta-\omega t)}\right|_{r=W}\ , \end{aligned}$$

and give rise to

$$\phi|_{r=0} = 0 = \phi|_{r=W} \ , \qquad \phi^{(1)}|_{r=0} = 0 = \phi^{(1)}|_{r=W} \ . \tag{B 3}$$

Let us remind that, from the normal-mode decomposition of $\Delta(\theta, t)$ and the following discussion, the membrane deformation is given by a superposition of modes interfering into a stationary wave:

$$\begin{aligned}\Delta(\theta,t) &= \sum_{n\in\mathbb{N}} \left\{ \xi_n \left[\mathrm{e}^{\mathrm{i}(n\theta-\omega_n t)} + \mathrm{e}^{\mathrm{i}(-n\theta-\omega_n t)} \right] + \xi_n^\star \left[\mathrm{e}^{\mathrm{i}(-n\theta+\omega_n^\star t)} + \mathrm{e}^{\mathrm{i}(n\theta+\omega_n^\star t)} \right] \right\} \\ &= 4 \sum_{n\in\mathbb{N}} \cos(n\theta) \left[\mathrm{Re}(\xi_n) \cos(\mathrm{Re}(\omega_n) t) + \mathrm{Im}(\xi_n) \sin(\mathrm{Re}(\omega_n) t) \right] \mathrm{e}^{\mathrm{Im}(\omega_n) t} \\ &= 4 \sum_{n\in\mathbb{N}} |\xi_n| \cos(n\theta) \cos[\mathrm{Re}(\omega_n) t + \sigma_\xi] \mathrm{e}^{\mathrm{Im}(\omega_n) t} \ ,\end{aligned} \tag{B 4}$$

which defines the phase shift σ_ξ mentioned in table 2 and in section 4.3.

Then we have to remember that the membrane moves with the same local and instantaneous value of the fluid velocity. In our Eulerian formalism, the full Lagrangian motion must be projected on the radial direction, i.e.:

$$\begin{aligned} &\frac{\partial \mathcal{R}(\theta,t)}{\partial t} = u_r(R,\theta,t) \implies \frac{\partial \Delta(\theta,t)}{\partial t} = \frac{1}{R} \frac{\partial \psi(R,\theta,t)}{\partial \theta} \\ &\implies -\mathrm{i} \sum_{n=-\infty}^{+\infty} \omega_n \xi_n \mathrm{e}^{\mathrm{i}(n\theta-\omega_n t)} = \frac{\mathrm{i}}{R} \sum_{n=-\infty}^{+\infty} n \phi_n(R) \mathrm{e}^{\mathrm{i}(n\theta-\omega_n t)} \\ &\implies \xi_n = -\frac{n}{R\omega_n} \phi_n(R) \ . \end{aligned} \tag{B 5}$$

Analogously, from (A 4), for the elongation we have:

$$\begin{aligned} &\frac{\partial \tilde{\chi}(\theta,t)}{\partial t} = \frac{1}{R_0 R} \left(\frac{\partial}{\partial \theta} - R \frac{\partial^2}{\partial r \partial \theta} \right) \psi \Big|_{(R,\theta,t)} \\ &\implies -\mathrm{i} \sum_n \omega_n \gamma_n \mathrm{e}^{\mathrm{i}(n\theta-\omega_n t)} = \frac{\mathrm{i}}{R_0 R} \sum_n n \left[\phi_n - R\phi_n^{(1)} \right] \Big|_R \mathrm{e}^{\mathrm{i}(n\theta-\omega_n t)} \\ &\implies \gamma_n = -\frac{n}{R_0 R \omega_n} \left[\phi_n(R) - R\phi_n^{(1)}(R) \right] \ . \end{aligned} \tag{B 6}$$

Similarly to (B 4), the stream function modes interfere into a stationary form:

$$\begin{aligned}\psi(r,\theta,t) &= \sum_{n\in\mathbb{N}} \Big\{\phi_n(r)\left[-\mathrm{e}^{\mathrm{i}(n\theta-\omega_n t)} + \mathrm{e}^{\mathrm{i}(-n\theta-\omega_n t)}\right] + \phi_n^\star(r)\left[-\mathrm{e}^{\mathrm{i}(-n\theta+\omega_n^\star t)} + \mathrm{e}^{\mathrm{i}(n\theta+\omega_n^\star t)}\right]\Big\}\\ &= -4\sum_{n\in\mathbb{N}} \sin(n\theta)\left[\mathrm{Re}(\phi_n(r))\sin(\mathrm{Re}(\omega_n)t) - \mathrm{Im}(\phi_n(r))\cos(\mathrm{Re}(\omega_n)t)\right]\mathrm{e}^{\mathrm{Im}(\omega_n)t}\\ &= -4\sum_{n\in\mathbb{N}} |\phi_n(r)|\sin(n\theta)\sin[\mathrm{Re}(\omega_n)t + \sigma_\phi(r)]\mathrm{e}^{\mathrm{Im}(\omega_n)t}\ , \qquad \text{(B 7)}\end{aligned}$$

where the phase shift $\sigma_\phi(r)$ from table 2 and section 4.3 must be computed at $r = R$. Of course, consistently with (B 5), one would find the same result by time-differentiating (B 4) and by defining $\sigma_\omega = \arctan[-\mathrm{Im}(\omega_n)/\mathrm{Re}(\omega_n)]$, with $\sigma_\phi(R) = \sigma_\xi + \sigma_\omega$.

Replacing (B 5–B 6) into (B 2), we get the equation

$$\begin{aligned}&\phi^{(4)}(r) + \frac{2}{r}\phi^{(3)}(r) + \left(-\frac{2n^2+1}{r^2} + \frac{\mathrm{i}\omega}{\nu}\right)\phi^{(2)}(r)\\ &+\left(\frac{2n^2+1}{r^3} + \frac{\mathrm{i}\omega}{\nu r}\right)\phi^{(1)}(r) + \left(\frac{n^4-4n^2}{r^4} - \frac{\mathrm{i}\omega n^2}{\nu r^2}\right)\phi(r)\\ &+\frac{\mathrm{i}n^2 E}{\mu R_0 R\omega}\left\{\left[\frac{1}{R}\left[n^2\left(1-\frac{R_0}{R}\right)+2\right]\phi(R) - 2\phi^{(1)}(R)\right]\frac{\delta(r-R)}{r}\right.\\ &\left.-\left[\left(1-\frac{R_0}{R} - 2\frac{r}{R} + \frac{rR_0}{R^2}\right)\phi(R) + r\phi^{(1)}(R)\right]\frac{\dot\delta(r-R)}{r}\right\} = 0 \qquad \text{(B 8)}\end{aligned}$$

(closed in ϕ), which can be either translated into the system (3.6,3.9–3.10), or nondimensionalised into:

$$\begin{aligned}&\phi^{(4)}(r_*) + \frac{2}{r_*}\phi^{(3)}(r_*) + \left(-\frac{2n^2+1}{r_*^2} + \frac{\mathrm{i}\omega_*}{\nu_*}\right)\phi^{(2)}(r_*)\\ &+\left(\frac{2n^2+1}{r_*^3} + \frac{\mathrm{i}\omega_*}{\nu_* r_*}\right)\phi^{(1)}(r_*) + \left(\frac{n^4-4n^2}{r_*^4} - \frac{\mathrm{i}\omega_* n^2}{\nu_* r_*^2}\right)\phi(r_*)\\ &+\frac{\mathrm{i}n^2}{\omega_*\nu_*(1-R_*)r_*}\left\{\left[\left[n^2(1-R_*)+2\right]\phi(1) - 2\phi^{(1)}(1)\right]\delta(r_*-1)\right.\\ &\left.-\left[(1-R_*-2r_*+r_*R_*)\phi(1) + r_*\phi^{(1)}(1)\right]\dot\delta(r_*-1)\right\} = 0\ . \qquad \text{(B 9)}\end{aligned}$$

Equation (B 9) then gives rise to (3.11) in both fluid domains, and to constraints (3.12–3.13). These latter are obtained via a single or double integration from $r_* = 1_-$ to 1_+. Notice in particular the relation

$$\lim_{\epsilon\to 0}\int_{1-\epsilon}^{1+\epsilon}\mathrm{d}r_\dagger \int_{1-\epsilon}^{r_\dagger}\mathrm{d}r_*\,\frac{1}{r_*}\dot\delta(r_*-1) = 1\ .$$

Appendix C. Details of the numerical procedure

The numerical procedure adopted to find ω consists in discretising (3.6) on the one-dimensional radial domain, and in interpreting it in terms of the discretised function $\phi_{[k]} \equiv \phi|_{r=r_k}$. We discretise both the internal ($0 < r < R$) and the external ($R < r < W$) regions into uniform intervals of constant size $\triangle r$ (thus $r_k = (k-1)r$), chosen such that $m-1 = R/\triangle r$ and $M-1 = W/\triangle r$ are integers. The leftmost node $k = 1$ is placed at the origin, the node $k = m$ is placed on the circle of radius $r_m = R$ which approximates the unperturbed membrane, and the rightmost node $k = M$ is placed just on the external wall. There are thus $m-1$ intervals in the internal region, $M-m$ in the external one, and $M-1$ in total, so that M is the dimension of the vector $\phi_{[k]}$. Equation (3.11) is then evaluated at each node, using centred finite-difference schemes. The boundary and interface nodes $k = 1, m, M$ must be treated separately, because the discrete derivatives have a different form there. The upshot is the linear homogeneous system

$$\sum_{l=1}^{M} A_{kl}\phi_{[l]} = 0 \;, \tag{C 1}$$

which possesses a non-trivial solution only if the matrix determinant is zero. The equation $\det \mathtt{A} = 0$ has been solved for ω numerically by means of a MATLAB code, and the relevant solution is the one with the largest imaginary part (viz. the least-negative one, all solutions being below the real axis), i.e. with the smallest damping rate or the largest decay time. More precisely, in the framework of sparse matrices, we have plotted and maximized the condition number (ratio of the largest to the smallest singular value) in the complex ω plane.

The matrix A_{kl} has been expressed in terms of the discrete derivatives used to replace the function $\phi(r)$ with the vector $\phi_{[k]}$. Let us specify that at the nodes $k = 1, 2, m-1, m, m+1, M-1, M$ we renounce to impose the differential equation, because we have to use the corresponding lines of the matrix to impose boundary and jump conditions. Namely, at the interface the function is continuous by construction, and we use the lines $k = m - 1, m, m + 1$ to impose the continuity of the first derivative (3.8) and the jumps of the second and third derivatives (3.9–3.10). From (3.7), the lines $k = 1$ and $k = M$ are used to impose the vanishing of the function, and similarly at $k = 2$ and $k = M - 1$ for the first derivative (the only exception being that, to obtain the free-slip cases in figure 2, we use this latter line to impose constraint (4.1)). For the discrete derivatives we use the standard formulae, centred whenever possible and suitably modified near the boundaries, with an overall precision of $O(\triangle r^2)$.

The first derivative is assumed

$$\phi^{(1)}_{[k]} \mapsto \triangle r^{-1}(\phi_{[k+1]} - \phi_{[k-1]})\ ,$$

except at the nodes $k = 1$ and $k = M$ where it is

$$\phi^{(1)+}_{[k]} \mapsto (2\triangle r)^{-1}(-\phi_{[k+2]} + 4\phi_{[k+1]} - 3\phi_{[k]})$$

and

$$\phi^{(1)-}_{[k]} \mapsto (2\triangle r)^{-1}(3\phi_{[k]} - 4\phi_{[k-1]} + \phi_{[k-2]})$$

respectively (both the latter expressions are also used at $k = m$ to impose the continuity constraint).

The second derivative is assumed

$$\phi^{(2)}_{[k]} \mapsto \triangle r^{-2}(\phi_{[k+1]} - 2\phi_{[k]} + \phi_{[k-1]})\ ,$$

except at the node $k = m$ (and also $k = M$ in the case of free-slip wall conditions) where the two expressions

$$\phi^{(2)+}_{[k]} \mapsto \triangle r^{-2}(-\phi_{[k+3]} + 4\phi_{[k+2]} - 5\phi_{[k+1]} + 2\phi_{[k]})$$

and

$$\phi^{(2)-}_{[k]} \mapsto \triangle r^{-2}(2\phi_{[k]} - 5\phi_{[k-1]} + 4\phi_{[k-2]} - \phi_{[k-3]})$$

are used to impose the jump constraint.

The third derivative is assumed

$$\phi^{(3)}_{[k]} \mapsto 2^{-1}\triangle r^{-3}(\phi_{[k+2]} - 2\phi_{[k+1]} + 2\phi_{[k-1]} - \phi_{[k-2]}) \ ,$$

except at the node $k = m$ where the two expressions

$$\phi^{(3)+}_{[k]} \mapsto 2^{-1}\triangle r^{-3}(-3\phi_{[k+4]} + 14\phi_{[k+3]} - 24\phi_{[k+2]} + 18\phi_{[k+1]} - 5\phi_{[k]})$$

and

$$\phi^{(3)-}_{[k]} \mapsto 2^{-1}\triangle r^{-3}(5\phi_{[k]} - 18\phi_{[k-1]} + 24\phi_{[k-2]} - 14\phi_{[k-3]} + 3\phi_{[k-4]})$$

hold respectively.

The fourth derivative is assumed

$$\phi^{(4)}_{[k]} \mapsto \triangle r^{-4}(\phi_{[k+2]} - 4\phi_{[k+1]} + 6\phi_{[k]} - 4\phi_{[k-1]} + \phi_{[k-2]}) \ .$$

In the end, here are the non-zero terms of the sparse matrix `A`:

- row $k = 1$: $A_{1,1} = 1$;
- row $k = 2$: $A_{2,1} = -3$, $A_{2,2} = 4$, $A_{2,3} = -1$;
- rows $3 \le k \le m - 2$ and $m + 2 \le k \le M - 2$: $A_{k,k-2} = 1 - 1/K$, $A_{k,k-1} = -4 + 2/K - (2n^2+1)/K^2 - (2n^2+1)/2K^3 + \mathrm{i}\omega_* q^2/\nu_* - \mathrm{i}\omega_* q^2/2\nu_* K$, $A_{k,k} = 6 + 2(2n^2+1)/K^2 + (n^4 - 4n^2)/K^4 - 2\mathrm{i}\omega_* q^2/\nu_* - \mathrm{i}\omega_* n^2 q^2/\nu_* K^2$, $A_{k,k+1} = -4 - 2/K - (2n^2+1)/K^2 + (2n^2+1)/2K^3 + \mathrm{i}\omega_* q^2/\nu_* + \mathrm{i}\omega_* q^2/2\nu_* K$, $A_{k,k+2} = 1 + 1/K$;
- row $k = m - 1$: $A_{m-1,m-3} = -A_{m-1,m+3} = 1$, $A_{m-1,m-2} = -A_{m-1,m+2} = -4$, $A_{m-1,m-1} = -A_{m-1,m+1} = 5 + \mathrm{i}n^2 abq/2\nu_*\omega_*(1-R_*)$, $A_{m-1,m} = \mathrm{i}n^2 aq^2/\nu_*\omega_*(1-R_*)$;
- row $k = m$: $A_{m,m-2} = A_{m,m+2} = 1$, $A_{m,m-1} = A_{m,m+1} = -4$, $A_{m,m} = 6$;
- row $k = m + 1$: $A_{m+1,m-4} = A_{m+1,m+4} = 3/2$, $A_{m+1,m-3} = A_{m-1,m+3} = -7$,

$A_{m+1,m-2} = A_{m+1,m+2} = 12$, $A_{m+1,m-1} = A_{m+1,m+1} = -9$, $A_{m+1,m} = 5 - \mathrm{i}n^2(n^2 - 1)q^3/\nu_*\omega_*$;

- row $k = M - 1$: $A_{M-1,M-3} = -(1-c)$, $A_{M-1,M-2} = c + [4 - 1/2(M-1)](1-c)$, $A_{M-1,M-1} = -4c + [-5 + 4/2(M-1)](1-c)$, $A_{M-1,M} = 3c + [2 - 3/2(M-1)](1-c)$;
- row $k = M$: $A_{M,M} = 1$.

Here, $q = \triangle r/R$, $K = k - 1$, and a, b, c are Boolean indicators. Namely, $a = 0$ only for droplets (section 5.1) and $= 1$ otherwise; $b = 0$ only in the case of purely-radial transport (section 5.2) and $= 1$ otherwise; $c = 0$ only in situations of free-slip external wall (part of section 4.1) and $= 1$ otherwise.

References

Abi Chebel, N., Vejražka, J., Masbernat, O. & Risso, F. 2012 Shape oscillations of an oil drop rising in water: effect of surface contamination. *J. Fluid Mech.* **702**, 533–542.

Biben, T., Farutin, A. & Misbah, C. 2011 Three-dimensional vesicles under shear flow: Numerical study of dynamics and phase diagram. *Phys. Rev. E* **83** (031921).

Boedec, G., Jaeger, M. & Leonetti, M. 2012 Settling of a vesicle in the limit of quasispherical shapes. *J. Fluid Mech.* **690**, 227–261.

Breyiannis, G. & Pozrikidis, C. 2000 Simple shear flow of suspensions of elastic capsules. *Theoret. Comput. Fluid Dyn.* **13**, 327–347.

Chandrasekhar, S. 1961 *Hydrodynamic and hydromagnetic stability*. Oxford University Press.

Cottet, G.-H. & Maitre, E. 2006 A level set method for fluid-structure interactions with immersed surfaces. *Math. Mod. Meth. App. Sc.* **16** (3), 415–438.

Fraser, K. H., Tskain, M. E., Griffith, B. P. & Wu, Z. J. 2011 The use of computational fluid dynamics in the development of ventricular assist devices. *Med. Eng. Phys.* **33**, 263–280.

Ghigliotti, G., Biben, T. & Misbah, C. 2010 Rheology of a dilute two-dimensional suspension of vesicles. *J. Fluid Mech.* **653**, 489–518.

Gray, A. 1997 Curvature of curves in the plane. In *Modern Differential Geometry of Curves and Surfaces with Mathematica*.

Greengard, L. & Kropinski, M. C. 1998 An integral equation approach to the incompressible Navier-Stokes equations in two dimensions. *SIAM J. Sci. Comput.* **20** (1), 318–336.

Hu, X.-Q., Salsac, A.-V. & Barthès-Biesel, D. 2012 Flow of a spherical capsule in a pore with circular or square cross-section. *J. Fluid Mech.* **705**, 176–194.

Jiang, S., Kropinski, M. C. A. & Quaife, B. D. 2013 Second kind integral equation formulations for the modified biharmonic equation and its applications. *J. Comput. Phys.* **249**, 113–126.

Jiang, S., Veerapaneni, S. & Greengard, L. 2012 Integral equation methods for unsteady Stokes flow in two dimensions. *SIAM J. Sci. Comput.* **34** (4), A2197–A2219.

Kelvin, Lord 1890 Oscillations of a liquid sphere. In *Mathematical and physical papers*. Clay and Sons.

Kim, Y. & Lai, M.-C. 2010 Simulating the dynamics of inextensible vesicles by the penalty immersed boundary method. *J. Comput. Phys.* **229**, 4840–4853.

Kropinski, M. C. A. & Lushi, E. 2011 Efficient numerical methods for multiple surfactant-coated bubbles in a two-dimensional Stokes flow. *J. Comput. Phys.* **230**, 4466–4487.

Lac, E., Morel, A. & Barthès-Biesel, D. 2007 Hydrodynamic interaction between two identical capsules in simple shear flow. *J. Fluid Mech.* **573**, 149–169.

Lamb, H. 1932 *Hydrodynamics*, 6th edn. Cambridge University Press.

Le, D.-V., Khoo, B. C. & Peraire, J. 2006 An immersed interface method for viscous incompressible flows involving rigid and flexible boundaries. *J. Comput. Phys.* **220**, 109–138.

Lee, L. & Leveque, R. J. 2003 An immersed interface method for incompressible Navier–Stokes equations. *SIAM J. Sci. Comput.* **25** (3), 832–856.

Lu, H.-L. & Apfel, R. E. 1991 Shape oscillations of drops in the presence of surfactants. *J. Fluid Mech.* **222**, 351–368.

Mendez, S., Gibaud, E. & Nicoud, F. 2014 An unstructured solver for simulations of deformable particles in flows at arbitrary Reynolds numbers. *J. Comput. Phys.* **256** (1), 465–483.

Miller, C. A. & Scriven, L. E. 1968 The oscillations of a fluid droplet immersed in another fluid. *J. Fluid Mech.* **32** (3), 417–435.

Moureau, V., Domingo, P. & Vervisch, L. 2011*a* Design of a massively parallel CFD code for complex geometries. *Comp. Rend. Méc.* **339** (2-3), 141–148.

Moureau, V., Domingo, P. & Vervisch, L. 2011*b* From large-eddy simulation to direct numerical simulation of a lean premixed swirl flame: Filtered laminar flame-PDF modelling. *Comput. Fluids* **158**, 1340–1357.

Padrino, J. C., Funada, T. & Joseph, D. D. 2008 Purely irrotational theories for the viscous effects on the oscillations of drops and bubbles. *Int. J. Multiphase Flow* **34** (1), 61–75.

Peng, Z., Asaro, R. J. & Zhu, Q. 2011 Multiscale modelling of erythrocytes in Stokes flow. *J. Fluid Mech.* **686**, 299–337.

Peskin, C. S. 1977 Numerical analysis of blood flow in the heart. *J. Comput. Phys.* **25**, 220–252.

PESKIN, C. S. 2002 The immersed boundary method. *Acta Num.* **11**, 479–517.

POZRIKIDIS, C. 1992 *Boundary Integral and Singularity Methods for Linearized Viscous Flow*. Cambridge University Press.

POZRIKIDIS, C. 1995 Finite deformation of liquid capsules enclosed by elastic membranes in simple shear flow. *J. Fluid Mech.* **297**, 123–152.

POZRIKIDIS, C. 2010 *Computational Hydrodynamics of Capsules and Biological Cells*. Boca Raton: Chapman & Hall/CRC.

PROSPERETTI, A. 1980*a* Free oscillations of drops and bubbles: the initial-value problem. *J. Fluid Mech.* **100** (2), 333–347.

PROSPERETTI, A. 1980*b* Normal-mode analysis for the oscillations of a viscous liquid drop in an immiscicle liquid. *J. Méc.* **19** (1), 149–182.

RAYLEIGH, LORD 1896 *The theory of sound*, 2nd edn. MacMillan.

ROCHAL, S. B., LORMAN, V. L. & MENNESSIER, G. 2005 Viscoelastic dynamics of spherical composite vesicles. *Phys. Rev. E* **71** (021905).

SALAC, D. & MIKSIS, M. 2011 A level set projection model of lipid vesicles in general flows. *J. Comput. Phys.* **230**, 8192–8215.

SALAC, D. & MIKSIS, M. 2012 Reynolds number effects on lipid vesicles. *J. Fluid Mech.* **711**, 122–146.

SOHN, J. S., TSENG, Y.-H., LI, S., VOIGT, A. & LOWENGRUB, J. S. 2010 Dynamics of multicomponent vesicles in a viscous fluid. *J. Comput. Phys.* **229**, 119–144.

SONG, P., HU, D. & ZHANG, P. 2008 Numerical simulation of fluid membranes in two-dimensional space. *Commun. Comput. Phys.* **3** (4), 794–821.

TAN, Z., LE, D. V., LI, Z., LIM, K. M. & KHOO, B. C. 2008 An immersed interface method for solving incompressible viscous flows with piecewise constant viscosity across a moving elastic membrane. *J. Comput. Phys.* **227**, 9955–9983.

Tu, C. & Peskin, C. S. 1992 Stability and instability in the computation of flows with moving immersed boundaries: a comparison of three methods. *SIAM J. Sci. Stat. Comput.* **13** (6), 1361–1378.

Veerapaneni, S. K., Gueyffier, D., Zorin, D. & Biros, G. 2009 A boundary integral method for simulating the dynamics of inextensible vesicles suspended in a viscous fluid in 2D. *J. Comput. Phys.* **228**, 2334–2353.

Veerapaneni, S. K., Rahimian, A., Biros, G. & Zorin, D. 2011 A fast algorithm for simulating vesicle flows in three dimensions. *J. Comput. Phys.* **230**, 5610–5634.

Walter, J., Salsac, A.-V. & Barthès-Biesel, D. 2011 Ellipsoidal capsules in simple shear flow: prolate versus oblate initial shapes. *J. Fluid Mech.* **676**, 318–347.

Woolfenden, H. C. & Blyth, M. G. 2011 Motion of a two-dimensional elastic capsule in a branching channel flow. *J. Fluid Mech.* **669**, 3–31.

Yazdani, A. Z. K. & Bagchi, P. 2013 Influence of membrane viscosity on capsule dynamics in shear flow. *J. Fluid Mech.* **718**, 569–595.

Zhao, H., Isfahani, A. H. G., Olson, L. N. & Freund, J. B. 2010 A spectral boundary integral method for flowing blood cells. *J. Comput. Phys.* **229**, 3726–3744.

Zhao, H. & Shaqfeh, E. S. 2011 The dynamics of a vesicle in simple shear flow. *J. Fluid Mech.* **674**, 578–604.